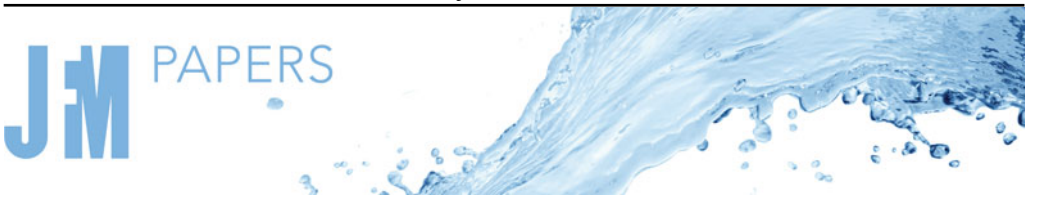
J. Fluid Mech. (2026), *vol.* 1042, A3, doi:10.1017/jfm.2026.11934



Global linear stability analysis framework for supercritical fluid flows

Siyu Ding[1], **Longfei Wang**[1], **Zikang Weng**[2], **Qingzhou Lu**[1], **Chih-Yung Wen**[3] and **Xingjian Wang**[1]

[1]Department of Energy and Power Engineering, Tsinghua University, Beijing 100084, PR China

[2]Department of Mathematical Sciences, Tsinghua University, Beijing 100084, PR China

[3]Department of Aeronautical and Aviation Engineering, The Hong Kong Polytechnic University, Kowloon, Hong Kong

Corresponding author: Xingjian Wang, xingjianwang@tsinghua.edu.cn

(Received 17 November 2025 UTC; revised 7 June 2026 UTC; accepted 6 July 2026 UTC)

Supercritical fluid flows exhibit complex dynamics and stability characteristics because of drastic thermophysical property variations across the pseudo-boiling line. Conventional stability analysis methods, primarily developed for ideal gases at low pressures, cannot be directly applied to supercritical flows. The present study establishes a unified framework of global linear stability analysis (GLSA) suitable for supercritical fluid flows for the first time. The framework incorporates real-fluid effects in terms of a cubic equation of state and detailed treatment of thermodynamic and transport properties, and integrates both energy and species transport equations into the linearised governing equations. For demonstration, the developed GLSA framework is implemented to examine the stability characteristics of jets in crossflow at different supercritical pressures and momentum flux ratios (J). Global linear stability analysis provides quantitative assessments of growth rates of dynamical events by recognising large eigenvalues and associated eigenmodes. The results show that the real-fluid modification is critical to accurately capture the growth rate magnitude of unstable modes. At low supercritical pressure, the position of the dominant GLSA eigenmode shifts from near the nozzle exit to farther downstream, accompanied by a significant reduction in growth rate magnitude. This shift is in alignment with the transition from global to convective instability in the jet upstream shear layer, where the Rayleigh–Taylor instability is enhanced owing to a pronounced density gradient. Furthermore, the GLSA eigenvalue spectrum quantifies the distinction in stability characteristics induced by the real-fluid effect even under identical J. The novel real-fluid algorithm can be extended to the stability analysis of many other supercritical fluid flows.

Key words: absolute/convective instability, jets, compressible turbulence

© The Author(s), 2026. Published by Cambridge University Press.

https://doi.org/10.1017/jfm.2026.11934 Published online by Cambridge University Press

1. Introduction

Supercritical fluids play a significant role in a variety of industrial applications, such as liquid rocket engines (Yang 2000; Wang *et al.* 2019), regenerative cooling (Xie *et al.* 2022) and thermal power cycles (White *et al.* 2021; Cao *et al.* 2023*b*). Fluids at supercritical pressure demonstrate numerous distinctive thermodynamic behaviours, including reduced viscosity, negligible surface tension, enhanced diffusivity and vanishment of the conventional gas–liquid interface (Yang 2000; Dahms & Oefelein 2013; Guardone *et al.* 2024). Additionally, thermodynamic and transport properties exhibit anomalous variations near the critical point and across the pseudo-boiling line (Wan *et al.* 2025). Figure 1 shows such behaviour using N-dodecane as an example (critical point:1.817 MPa,658.1K). At a pressure close to the critical value of $p_r = p_a/p_{cr} = 1.01$, the thermophysical properties of dodecane exhibit pronounced nonlinear variations near the pseudo-boiling point (where the maximum specific heat at constant pressure occurs, approximately at 659K). This behaviour is recognised as the real-fluid effect of supercritical fluids (Zong *et al.* 2004; Ding *et al.* 2024*a*), which triggers many distinct flow characteristics from the ideal-gas counterpart. Linear stability analysis is a valuable tool to describe the instability evolution and laminar to turbulence transition in fluid flows. However, most existing studies have focused on the stability analysis of ideal gases and have not taken into account real-fluid effects, which are necessary for supercritical flows. To this end, we develop a systematic framework of global linear stability analysis (GLSA) for supercritical fluid flows and further demonstrates its application to a supercritical jet in crossflow (JICF).

Linear stability analysis can be broadly categorised into two types: local linear stability analysis (LLSA) and GLSA (Huerre & Monkewitz 1990). Local linear stability analysis typically characterises the local impulse response of the system under the parallel-flow assumption at each streamwise location. Several studies (Fu & Yang 2016; Fu *et al.* 2018; Ren *et al.* 2018, 2019; Wang *et al.* 2022) have conducted LLSA on supercritical fluid flows. Ren *et al.* (2018) analysed the stability in CO_2 Poiseuille flow at supercritical pressures and identified inflectional profiles in the velocity distribution, attributed to strong property gradients under transcritical conditions. Wang *et al.* (2022) investigated the stability of a supercritical-pressure nitrogen mixing layer and demonstrated that near the critical point, the maximum spatial growth rate and the most unstable frequency, derived from the real-fluid density profile, are significantly lower than those predicted under the ideal-gas assumption. This discrepancy is explained by the emergence of an inflection point in the density distribution within the mixing layer. Although LLSA has been employed to explore the stability of supercritical fluid flows, the parallel-flow approximation in LLSA is not strictly applicable to flows with distinct three-dimensional characteristics, such as a JICF (or transverse jet), which is frequently employed for fuel injection in advanced propulsion systems.

In contrast, GLSA directly deals with the stability characteristics of the entire flow field (Huerre & Monkewitz 1990; Theofilis 2011). It was initially introduced in Pierrehumbert & Widnall (1982) and subsequently found widespread application in the stability analysis of incompressible flows (Obrist & Schmid 2003; Barkley 2006; Kervik *et al.* 2007; Sipp & Lebedev 2007; Bagheri *et al.* 2009; Regan & Mahesh 2017; Canton *et al.* 2017). Barkley (2006) conducted a GLSA of the mean flow arising from laminar vortex shedding behind a circular cylinder across a range of Reynolds numbers (46–180). Results revealed that the eigenfrequency of the mean flow is virtually correlated with the Strouhal number of the vortex shedding. Kervik *et al.* (2007) employed a set of two-dimensional global eigenmodes as a projection basis to analyse the flow dynamics and construct a

https://doi.org/10.1017/jfm.2026.11934 Published online by Cambridge University Press

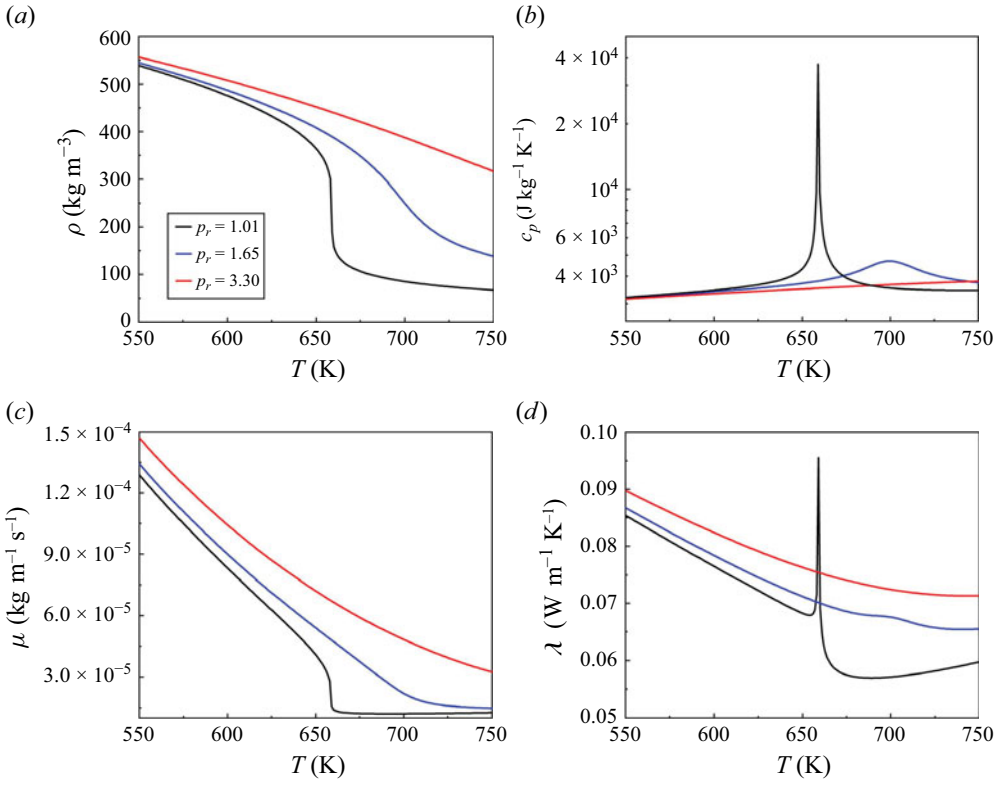


Figure 1. Property variations of dodecane at different supercritical pressures: (*a*) density, (*b*) specific heat capacity at constant pressure, (*c*) dynamic viscosity, (*d*) thermal conductivity.

reduced-order model for control applications in a prototype separated boundary-layer flow. An optimal growth analysis demonstrated that a linear combination of these highly non-normal global eigenmodes effectively captures the evolution of localised disturbances. The GLSA of incompressible coaxial jets by Canton *et al.* (2017) demonstrated that the dominant behaviour of alternating vortex shedding from the duct wall originates from an unstable global mode of the axisymmetric base flow, rather than from the inherent convective nature of jet flow instabilities. As a canonical three-dimensional flow configuration, JICF has also been the subject of GLSA in previous studies.

Jet in crossflow involves a transverse jet injected perpendicularly into a crossflow. This fundamental flow configuration has been extensively investigated over decades, driven by its wide-ranging relevance to propulsion systems in engineering applications (Karagozian 2010; Mahesh 2013). Extensive experiments have revealed that the jet's upstream shear-layer (USL) transitions from convective instability to absolute/global instability as the jet-to-crossflow momentum flux ratio (J) gradually decreases (Megerian *et al.* 2007; Davitian *et al.* 2010; Getsinger *et al.* 2014) (with critical $J \approx 10$). Experiments have evidenced that low-amplitude external excitations of JICF with a convectively unstable USL can significantly enhance mixing efficiency (Narayanan *et al.* 2003; Getsinger *et al.* 2012). In the case of global instability, in contrast, high-amplitude excitations prove ineffective in suppressing the dominant instability mode or improving jet penetration and mixing performance (M'Closkey *et al.* 2002; Shapiro *et al.* 2006; Getsinger *et al.* 2012).

https://doi.org/10.1017/jfm.2026.11934 Published online by Cambridge University Press

Linear stability analysis provides further insight into the stability characteristics of JICF. Alves *et al.* (2007, 2008) and Amini (2018) used LLSA to investigate the shear-layer stability of JICF within the convectively unstable regime and examined the maximum spatial growth rate of disturbances. However, as previously noted, JICF represents a classic three-dimensional flow configuration, rendering the suitability of LLSA to restricted situations. On the other hand, GLSA has shown effectiveness in resolving the intricate USL instabilities of JICF (Bagheri *et al.* 2009; Peplinski *et al.* 2015; Regan & Mahesh 2017). Bagheri *et al.* (2009) performed a GLSA on a three-dimensional base flow of JICF and revealed the presence of high-frequency unstable global eigenmodes related to shear-layer instabilities on the counter-rotating vortex pair (CVP), as well as low-frequency modes linked to the periodic shedding of vortices in the jet wake. Regan & Mahesh (2017) employed GLSA on JICFs at a jet Reynolds number of $Re_j = 2000$ and captured the transition from global to convective instability in the USL reported by Megerian *et al.* (2007), within the range of velocity ratio (R) from 2 to 4. Specifically, the USL instability prevails at $R = 2$, while the downstream shear-layer instability becomes predominant at $R = 4$. Despite numerous advancements in the literature, the existing GLSA studies on JICF have been mainly conducted at low to moderate pressures with incompressible ideal gas as the working fluid, which cannot be employed to study JICF at supercritical pressures (hereinafter, supercritical JICF) with strong real-fluid effects. Modifications of the base flow and the stability analysis algorithm are necessary to account for real-fluid effects, such as compressibility and abrupt property variations.

Compressibility effects have been considered in numerous studies of the stability analysis of high-speed flows (Schmidt & Rist 2011; Kumar *et al.* 2014; Luo *et al.* 2019; Hao *et al.* 2021; Cao *et al.* 2023*a*; Liu *et al.* 2024). Schmidt & Rist (2011) investigated the linear stability of compressible flow within a streamwise corner. They compared base flows at three Mach numbers (Ma), corresponding to the incompressible limit, a subsonic regime and a supersonic regime. In the supersonic case, they identified an inviscid corner mode exhibiting odd symmetry. This mode, while absent in the subsonic regime, demonstrated a higher amplification rate than its symmetric counterpart. Through GLSA, Hao *et al.* (2021) demonstrated that the shock-induced separated flow in a supersonic flow (Mach 7.7) over a two-dimensional compression corner becomes unstable beyond a specific critical ramp angle. They further reported that while an increase in wall temperature substantially enlarges the separation region, it only leads to a slight increase in the critical angle. These investigations primarily address compressibility effects of ideal gases under high-Mach-number conditions, which, however, differ fundamentally from those considered in the present study, namely, compressibility effects induced by the drastic property variations of real fluids at supercritical pressures, despite low Mach numbers. To the best of the authors' knowledge, no existing GLSA research has been reported for supercritical fluid flow. Such flow is of great significance in response to the increasing demands for higher thermal efficiency and greater thrust in advanced propulsion systems (Wang *et al.* 2018), where the influence of real-fluid effects is critical.

The present study develops a novel GLSA framework for supercritical fluid with detailed treatment of abnormal thermophysical property variations. Real-fluid effects are carefully considered by incorporating a cubic equation of state (EOS) and fundamental thermodynamics and transport theories, which are employed in both the numerical simulation of the base flow and the GLSA governing equations. For demonstration, the framework is implemented to explore the stability characteristics of transverse jets at supercritical pressures.

https://doi.org/10.1017/jfm.2026.11934 Published online by Cambridge University Press

2. Global linear stability analysis framework for supercritical fluids

Global linear stability analysis investigates the dynamic response of a base flow under external perturbations (Theofilis 2011). This section first presents the theoretical and numerical formulation for the base flow, then derives the GLSA algorithm for supercritical flows, and concludes with validations of the proposed algorithm.

2.1. *Theoretical formulation for base flow*

The theoretical framework of the base flow is designed to address supercritical fluid dynamics across a broad spectrum of relevant thermodynamic conditions. In the absence of body forces, the conservation equations of the base flow can be expressed in their primitive form as follows.

Mass:

$$\frac{\partial \rho}{\partial t} + \rho \frac{\partial u_j}{\partial x_j} + u_j \frac{\partial \rho}{\partial x_j} = 0; \tag{2.1}$$

momentum:

$$\frac{\partial u_i}{\partial t} + u_j \frac{\partial u_i}{\partial x_j} + \frac{1}{\rho}\frac{\partial p}{\partial x_i} - \frac{1}{\rho}\frac{\partial \tau_{ij}}{\partial x_j} = 0; \tag{2.2}$$

energy:

$$\rho \frac{\partial e}{\partial t} + \rho u_j \frac{\partial e}{\partial x_j} + p \frac{\partial u_j}{\partial x_j} = \frac{\partial q_j}{\partial x_j} + \Phi; \tag{2.3}$$

species:

$$\rho \frac{\partial Y_k}{\partial t} + \rho u_j \frac{\partial Y_k}{\partial x_j} - \frac{\partial}{\partial x_j}\left(\rho D \frac{\partial Y_k}{\partial x_j}\right) = 0. \tag{2.4}$$

Here ρ, u, p and Y_k denote density, velocity, pressure and mass fraction of species k, respectively. The viscous stress tensor τ_{ij} is defined as

$$\tau_{ij} = \mu\left(\frac{\partial u_i}{\partial x_j} + \frac{\partial u_j}{\partial x_i} - \frac{2}{3}\delta_{ij}\frac{\partial u_l}{\partial x_l}\right), \tag{2.5}$$

where μ is dynamic viscosity. The bulk viscosity effect is neglected in this study, which is commonly adopted in prior investigations of supercritical fluid flows (Miller *et al.* 2001; Okong'o & Bellan 2002; Oefelein 2005; Ren *et al.* 2018). Here e, Φ, q_j and D denote specific internal energy, energy generated by viscous dissipation, heat flux and mass diffusivity, respectively. In this study, only the mass fraction of the jet (Y_1) needs to be considered in the governing equations, and the mass fraction of the crossflow (Y_2) can be determined as

$$Y_2 = 1 - Y_1. \tag{2.6}$$

The internal energy equation given in (2.3) is simplified by neglecting Φ and reformulated in terms of temperature, i.e.

$$\rho c_v\left(\frac{\partial T}{\partial t} + u_j \frac{\partial T}{\partial x_j}\right) + p\frac{\partial u_j}{\partial x_j} + \frac{\partial}{\partial x_j}\left(\lambda \frac{\partial T}{\partial x_j}\right) = 0, \tag{2.7}$$

where T, c_v and λ denote temperature, specific heat capacity at constant volume and thermal conductivity, respectively.

To close the governing equations above, an EOS is required to describe the thermodynamic relationship between pressure, temperature and volume. This study

https://doi.org/10.1017/jfm.2026.11934 Published online by Cambridge University Press

employs a widely used cubic EOS, i.e. the Peng–Robinson (PR) EOS,

$$p = \frac{R_0 T}{V - b} - \frac{\alpha}{V^2 + 2bV - b^2}, \tag{2.8}$$

where V corresponds to the molar volume and R_0 signifies the universal gas constant. The parameters α and b characterise the intermolecular attractive and repulsive forces, respectively. Modelling supercritical fluid flows presents unique challenges due to thermodynamic non-idealities and anomalous transport behaviours. To accurately capture these real-fluid effects, a robust evaluation framework for thermophysical properties is essential. Thermodynamic properties, such as speed of sound and enthalpy, are computed based on fundamental thermodynamic theories coupled with the PR EOS. Here c_v is expressed as the sum of an ideal-gas part and a departure function accounting for dense-fluid correction (Meng & Yang 2003):

$$c_v(T, \rho) = c_{v_0}(T) - \int_{\rho_0}^{\rho} \left[\frac{T}{\rho^2} \left(\frac{\partial^2 p}{\partial T^2} \right)_\rho \right]_T d\rho. \tag{2.9}$$

The partial derivative $(\partial^2 p/\partial T^2)_\rho$ in (2.9) is obtained by differentiating the PR EOS, as given in (2.8). Transport properties λ and μ are calculated as (Yang 2000; Huber *et al.* 2022)

$$\lambda(T, \rho) = \lambda_0(T) + \Delta\lambda(T, \rho) + \Delta\lambda_c(T, \rho), \tag{2.10}$$

$$\mu\,(T, \rho) = \mu_0\,(T) + \Delta\mu\,(T, \rho) + \Delta\mu_c\,(T, \rho). \tag{2.11}$$

In (2.10) and (2.11) the first term corresponds to the contribution in the dilute-gas limit, where only two-body molecular interactions are present and the value can be accurately predicted using kinetic theory. The second term, referred to as the residual contribution, accounts for the effects at elevated densities, including many-body collisions, molecular-velocity correlations and collisional transfer. The third term describes the behaviour in the critical region. Mass diffusivity is evaluated using the Takahashi method, which has been specifically calibrated for high-pressure conditions (Wang & Yang 2017; Wang *et al.* 2019). Its formulation can be expressed as

$$(D_{ij}\,p)^+ = \frac{0.00143\,T^{1.75}}{M_{ij}^{1/2}\left[(\Sigma_v)_i^{1/3} + (\Sigma_v)_j^{1/3}\right]^2}, \tag{2.12}$$

$$\frac{D_{ij}\,p}{(D_{ij}\,p)^+} = f\,(T_r,\, p_r)\,, \tag{2.13}$$

where $M_{ij} = 2((1/M_i) + (1/M_j))^{-1}$ and $(\Sigma_v)_i$ represents the sum of the diffusion volume increments for all constituent elements of component i, which can be obtained from reference tables. The dimensionless temperature T_r and dimensionless pressure p_r are obtained by normalising with respect to their critical values. The function $f(T_r, p_r)$ is determined via tabulation based on the graphical data provided in Poling *et al.* (2001). Following the described theoretical formulation, these thermodynamic and transport properties are pre-calculated and stored in a table for subsequent high-fidelity simulations to improve computational efficiency.

The theoretical framework aforementioned has been extensively employed in the simulation of supercritical fluid flows (Meng & Yang 2003; Meng *et al.* 2005; Wang *et al.* 2018). The numerical solver employs a pressure-based, finite-volume methodology,

https://doi.org/10.1017/jfm.2026.11934 Published online by Cambridge University Press

integrated with the pressure-implicit with splitting of operators algorithm for pressure–velocity coupling. Temporal discretisation is implemented using a bounded second-order implicit scheme, while spatial discretisation is performed with a second-order upwind scheme. The numerical method has been successfully implemented by Ding *et al.* (2024*a*,*b*) for JICF at supercritical pressures and the calculated results have been validated against the experimental data reported by Xue *et al.* (2011).

2.2. *The GLSA algorithm*

As previously discussed, the GLSA at supercritical pressures must account for the real-fluid effects induced by abnormal thermophysical variations, whereas the existing GLSA studies are constrained with an ideal-gas assumption in the literature. Consequently, it is essential to develop the governing equations of GLSA suitable for supercritical fluid flows. The derivation process is illustrated in the flowchart presented in figure 2(*a*). The governing equations are deduced by introducing a small perturbation over the base flow, followed by a linearisation process. Each primitive flow variable q is decomposed into two terms: a base state $\overline{q}$ and a small perturbation $\tilde{q}$:

$$q = \overline{q} + \tilde{q}. \tag{2.14}$$

By substituting (2.14) into (2.1), (2.2), (2.4) and (2.7), and subsequently neglecting higher-order $O(\tilde{q}^2)$ terms, the linearised governing equations for the perturbations are obtained as

$$\frac{\partial \tilde{\rho}}{\partial t} + \tilde{\rho}\frac{\partial \overline{u}_j}{\partial x_j} + \overline{\rho}\frac{\partial \tilde{u}_j}{\partial x_j} + \tilde{u}_j\frac{\partial \overline{\rho}}{\partial x_j} + \overline{u}_j\frac{\partial \tilde{\rho}}{\partial x_j} = 0, \tag{2.15}$$

$$\begin{aligned}
&\frac{\partial \widetilde{u}_i}{\partial t} + \widetilde{u}_j\frac{\partial \overline{u}_i}{\partial x_j} + \overline{u}_j\frac{\partial \widetilde{u}_i}{\partial x_j} - \frac{\widetilde{\rho}}{\overline{\rho}^2}\frac{\partial \overline{p}}{\partial x_i} + \frac{1}{\overline{\rho}}\frac{\partial \widetilde{p}}{\partial x_i} \\
&+\frac{\widetilde{\rho}}{\overline{\rho}^2}\left[\frac{\partial \overline{\mu}}{\partial x_i}\left(\frac{\partial \overline{u}_i}{\partial x_j} + \frac{\partial \overline{u}_j}{\partial x_i} - \frac{2}{3}\delta_{ij}\frac{\partial \overline{u}_i}{\partial x_j}\right) + \overline{\mu}\left(\frac{\partial^2 \overline{u}_i}{\partial x_j^2} + \frac{\partial^2 \overline{u}_j}{\partial x_i \partial x_j} - \frac{2}{3}\frac{\partial^2 \overline{u}_i}{\partial x_i^2}\right)\right] \\
&-\frac{1}{\rho}\left[\frac{\partial \overline{\mu}}{\partial x_j}\left(\frac{\partial \widetilde{u}_i}{\partial x_j} + \frac{\partial \widetilde{u}_j}{\partial x_i} - \frac{2}{3}\delta_{ij}\frac{\partial \widetilde{u}_i}{\partial x_j}\right) + \overline{\mu}\left(\frac{\partial^2 \widetilde{u}_i}{\partial x_j^2} + \frac{\partial^2 \widetilde{u}_j}{\partial x_i \partial x_j} - \frac{2}{3}\frac{\partial^2 \widetilde{u}_i}{\partial x_i^2}\right)\right] = 0,
\end{aligned} \tag{2.16}$$

$$\begin{aligned}
&\frac{\partial \tilde{T}}{\partial t} + \tilde{u}_j\frac{\partial \overline{T}}{\partial x_j} + \overline{u}_j\frac{\partial \tilde{T}}{\partial x_j} + \frac{1}{\overline{\rho}\,\overline{c_v}}\left(\tilde{p}\frac{\partial \overline{u}_j}{\partial x_j} - \frac{\overline{p}\tilde{\rho}}{\overline{\rho}}\frac{\partial \overline{u}_j}{\partial x_j} + \overline{p}\frac{\partial \tilde{u}_j}{\partial x_j}\right) \\
&-\frac{\tilde{\rho}}{\overline{\rho}^2\,\overline{c_v}}\left(\frac{\partial \overline{\lambda}}{\partial x_j}\frac{\partial \overline{T}}{\partial x_j} + \overline{\lambda}\frac{\partial^2 \overline{T}}{\partial x_j^2}\right) + \frac{1}{\overline{\rho}\,\overline{c_v}}\left(\frac{\partial \overline{\lambda}}{\partial x_j}\frac{\partial \tilde{T}}{\partial x_j} + \overline{\lambda}\frac{\partial^2 \tilde{T}}{\partial x_j^2}\right) = 0,
\end{aligned} \tag{2.17}$$

$$\frac{\partial \widetilde{Y}_1}{\partial t} + \widetilde{u}_j\frac{\partial \overline{Y_1}}{\partial x_j} + \overline{u}_j\frac{\partial \widetilde{Y}_1}{\partial x_j} + \frac{\tilde{\rho}\overline{D}}{\overline{\rho}^2}\frac{\partial \overline{\rho}}{\partial x_j}\frac{\partial \overline{Y_1}}{\partial x_j} - \frac{\overline{D}}{\overline{\rho}}\frac{\partial \tilde{\rho}}{\partial x_j}\frac{\partial \overline{Y_1}}{\partial x_j} - \frac{\overline{D}}{\overline{\rho}}\frac{\partial \overline{\rho}}{\partial x_j}\frac{\partial \widetilde{Y}_1}{\partial x_j} - \frac{\partial \overline{D}}{\partial x_j}\frac{\partial \widetilde{Y}_1}{\partial x_j} - \overline{D}\frac{\partial^2 \widetilde{Y}_1}{\partial x_j^2} = 0. \tag{2.18}$$

The vector of perturbed primitive variables can be written as $\tilde{\boldsymbol{q}} = (\tilde{\rho}, \tilde{u}, \tilde{v}, \tilde{w}, \tilde{T}, \tilde{Y}_1)^{\mathrm{T}}$, according to (2.15)–(2.18). The perturbed pressure $\tilde{p}$ is unknown and needs to be solved by perturbing the PR EOS. Before such an operation, the PR EOS is conveniently expressed in terms of the compressibility factor as

$$p = Z\rho RT, \tag{2.19}$$

where R is the specific gas constant and Z represents the compressibility factor. Equation (2.19) is broadly used to represent the concise form of real-fluid EOS, and the substitution

https://doi.org/10.1017/jfm.2026.11934 Published online by Cambridge University Press

of the PR EOS (2.8) leads to a cubic equation of Z (Poling *et al.* 2001; Lopez-Echeverry *et al.* 2017). Note that Z quantifies the departure from ideal-gas behaviour ($Z = 1$ for ideal gases) and exhibits a significant deviation from unity in supercritical fluid flows. Applying perturbations to all thermodynamic variables in (2.19) using (2.14), the perturbed equation after linearisation becomes

$$\tilde{p} = \overline{Z}\overline{\rho}\overline{R}\tilde{T} + \overline{ZRT}\tilde{\rho} + \overline{\rho}\overline{RT}\tilde{Z} + \overline{Z}\overline{\rho}\overline{T}\tilde{R}. \tag{2.20}$$

Here, we neglect the contributions of the last two terms ($\tilde{Z}$ and $\tilde{R}$) to the perturbed pressure, because of their relatively small magnitudes compared with perturbed density and temperature. It should be noted that the time-averaged properties $\overline{Z}$ and $\overline{R}$ are not constant but depend on the local primitive properties. Inserting (2.20) into (2.16) and (2.17) lead to

$$\begin{aligned}
&\frac{\partial \widetilde{u}_i}{\partial t} + \widetilde{u}_j\frac{\partial \overline{u}_i}{\partial x_j} + \overline{u}_j\frac{\partial \widetilde{u}_i}{\partial x_j} - \frac{\tilde{\rho}}{\overline{\rho}^2}\frac{\partial \overline{p}}{\partial x_i} + \overline{ZR}\frac{\partial \widetilde{T}}{\partial x_i} + \frac{\overline{ZRT}}{\overline{\rho}}\frac{\partial \tilde{\rho}}{\partial x_i} \\
&+\frac{\tilde{\rho}}{\overline{\rho}^2}\left[\frac{\partial \overline{\mu}}{\partial x_j}\left(\frac{\partial \overline{u}_i}{\partial x_j} + \frac{\partial \overline{u}_j}{\partial x_i} - \frac{2}{3}\delta_{ij}\frac{\partial \overline{u}_i}{\partial x_j}\right) + \overline{\mu}\left(\frac{\partial^2 \overline{u}_i}{\partial x_j^2} + \frac{\partial^2 \overline{u}_j}{\partial x_i \partial x_j} - \frac{2}{3}\frac{\partial^2 \overline{u}_i}{\partial x_i^2}\right)\right] \\
&-\frac{1}{\overline{\rho}}\left[\frac{\partial \overline{\mu}}{\partial x_j}\left(\frac{\partial \widetilde{u}_i}{\partial x_j} + \frac{\partial \widetilde{u}_j}{\partial x_i} - \frac{2}{3}\delta_{ij}\frac{\partial \widetilde{u}_i}{\partial x_j}\right) + \overline{\mu}\left(\frac{\partial^2 \widetilde{u}_i}{\partial x_j^2} + \frac{\partial^2 \widetilde{u}_j}{\partial x_i \partial x_j} - \frac{2}{3}\frac{\partial^2 \widetilde{u}_i}{\partial x_i^2}\right)\right] = 0,
\end{aligned} \tag{2.21}$$

$$\begin{aligned}
&\frac{\partial \widetilde{T}}{\partial t} + \widetilde{u}_j\frac{\partial \overline{T}}{\partial x_j} + \overline{u}_j\frac{\partial \widetilde{T}}{\partial x_j} + \frac{\overline{Z}\,\overline{R}\widetilde{T}}{\overline{c_v}}\frac{\partial \overline{u}_j}{\partial x_j} + \frac{\overline{Z}\tilde{\rho}\overline{R}\,\overline{T}}{\overline{\rho c_v}}\frac{\partial \overline{u}_j}{\partial x_j} - \frac{\overline{p}\tilde{\rho}}{\overline{\rho}^2\overline{c_v}}\frac{\partial \overline{u}_j}{\partial x_j} + \frac{\overline{p}}{\overline{\rho c_v}}\frac{\partial \widetilde{u}_j}{\partial x_j} \\
&-\frac{\tilde{\rho}}{\overline{\rho}^2\overline{c_v}}\left(\frac{\partial \overline{\lambda}}{\partial x_j}\frac{\partial \overline{T}}{\partial x_j} + \overline{\lambda}\frac{\partial^2 \overline{T}}{\partial x_j^2}\right) + \frac{1}{\overline{\rho c_v}}\left(\frac{\partial \overline{\lambda}}{\partial x_j}\frac{\partial \widetilde{T}}{\partial x_j} + \overline{\lambda}\frac{\partial^2 \widetilde{T}}{\partial x_j^2}\right) = 0.
\end{aligned} \tag{2.22}$$

Equations (2.15), (2.18), (2.21) and (2.22) collectively form a closed system governed by the linearised equations with respect to $\tilde{\boldsymbol{q}} = (\tilde{\rho}, \tilde{u}, \tilde{v}, \tilde{w}, \tilde{T}, \tilde{Y}_1)^{\mathrm{T}}$, which takes into account real-fluid effects by involving a real-fluid EOS and a detailed treatment of thermophysical property evaluations. Alternatively, the governing equations can be expressed in a vector form, i.e.

$$\frac{\partial \tilde{\boldsymbol{q}}}{\partial t} = \boldsymbol{A}\tilde{\boldsymbol{q}}, \tag{2.23}$$

where $\boldsymbol{A}$ is the linear operator and can be written in the following componentwise form:

$$\boldsymbol{A} = -\begin{pmatrix}
A_{\rho\rho} & A_{\rho u} & A_{\rho v} & A_{\rho w} & A_{\rho T} & A_{\rho Y_1} \\
A_{u\rho} & A_{uu} & A_{uv} & A_{uw} & A_{uT} & A_{uY_1} \\
A_{v\rho} & A_{vu} & A_{vv} & A_{vw} & A_{vT} & A_{vY_1} \\
A_{w\rho} & A_{wu} & A_{wv} & A_{ww} & A_{wT} & A_{wY_1} \\
A_{T\rho} & A_{Tu} & A_{Tv} & A_{Tw} & A_{TT} & A_{TY_1} \\
A_{Y_1\rho} & A_{Y_1u} & A_{Y_1v} & A_{Y_1w} & A_{Y_1T} & A_{Y_1Y_1}
\end{pmatrix}. \tag{2.24}$$

Here A_{ij} denotes the coefficient of variable j in the governing equation of variable i. The complete form, dimensions and discretisation method of $\boldsymbol{A}$ are provided in Appendix A. Note that $\overline{\mu}$, $\overline{Z}$, $\overline{R}$, $\overline{c_v}$, $\overline{\lambda}$ and $\overline{D}$ in these equations represent time-averaged values at each spatial point and depend on the local primitive variables (temperature and density) instead of assigning constant values. They are calculated using the real-fluid property evaluation

https://doi.org/10.1017/jfm.2026.11934 Published online by Cambridge University Press

methods described in § 2.1. The perturbed variables are expressed as the product of

$$\tilde{q}\,(x,\,y,\,z,\,t) = \hat{q}\,(x,\,y,\,z)\,\mathrm{e}^{\omega t}, \tag{2.25}$$

where $\hat{q}$ and ω are generally complex numbers, $\omega = \omega_r + i\omega_i$. The temporal growth rate and the frequency are determined by the real component ω_r and the imaginary component ω_i, respectively. Substituting (2.25) into (2.23) results in

$$\omega\hat{\boldsymbol{q}} = \boldsymbol{A}\hat{\boldsymbol{q}}. \tag{2.26}$$

Equation (2.26) represents a general formulation of GLSA that is applicable to a wide range of fluid flow problems, where real-fluid effects caused by abnormal property variations are carefully considered. More importantly, it can not only handle supercritical flows with heat transfer and multi-species mixing, but also study compressible and incompressible ideal-gas flows through proper simplifications. For example, the algorithm can be easily degenerated to the physical problems where incompressible fluid is involved. For single-component, isothermal and incompressible flows, $\overline{Z} = 1$, $\tilde{T} = \tilde{Y}_1 = 0$. Equations (2.15) and (2.16) can be simplified as follows:

$$\frac{\partial \tilde{u}_j}{\partial x_j} = 0, \tag{2.27}$$

$$\frac{\partial \tilde{u}_i}{\partial t} + \tilde{u}_j\frac{\partial \overline{u}_i}{\partial x_j} + \overline{u}_j\frac{\partial \tilde{u}_i}{\partial x_j} + \frac{1}{\rho}\frac{\partial \tilde{p}}{\partial x_i} - \frac{\mu}{\rho}\frac{\partial^2 \tilde{u}_i}{\partial x_j^2} = 0. \tag{2.28}$$

As a result, the perturbed vector $\tilde{\boldsymbol{q}}$ is simplified as $(\tilde{u},\tilde{v},\tilde{w},\tilde{p})^{\mathrm{T}}$, and the corresponding transformation process is shown in figure 2(*b*). The linear operator $\boldsymbol{A}^*$ takes the following componentwise form:

$$\boldsymbol{A}^* = -\begin{pmatrix} A_{uu} & A_{uv} & A_{uw} & A_{up} \\ A_{vu} & A_{vv} & A_{vw} & A_{vp} \\ A_{wu} & A_{wv} & A_{ww} & A_{wp} \\ A_{pu} & A_{pv} & A_{pw} & A_{pp} \end{pmatrix}. \tag{2.29}$$

The complete form of elemental matrices in (2.29) is provided in Appendix A. For simplicity, the two GLSA algorithms are hereafter referred to as the 'real-fluid algorithm' and 'incompressible-fluid algorithm', respectively. Figure 3 shows the schematic of complexity comparison between the two algorithms.

For general three-dimensional flows, the explicit construction of matrix $\boldsymbol{A}$ is computationally prohibitive due to its large dimension ($O(10^6 - 10^8)$). To alleviate the issue, a specialised matrix-free time-stepper method is utilised (Bagheri *et al.* 2009). The time-integration operator $\boldsymbol{B} = \mathrm{e}^{A\tau}$ is introduced to serve as a numerical representation for simulating the system of linear equations across a time interval τ. This process converts the most unstable eigenvalues into the most dominant ones, characterised by their maximal magnitude. The eigenvectors of matrices $\boldsymbol{A}$ and $\boldsymbol{B}$ are identical, whereas the eigenvalues of $\boldsymbol{A}(\omega)$ can be derived from the eigenvalues of $\boldsymbol{B}$ (denoted as σ) through the relation $\omega = \ln(\sigma)/\tau$. The computation of the leading (most unstable) eigenvalues and their associated eigenmodes is carried out via the implicitly restarted Arnoldi method (IRAM), utilising the ARPACK software library (Lehoucq *et al.* 1998). Specifically, the selection of τ involves balancing the time scale dictated by the Nyquist criterion with the need for adequate temporal separation of the Krylov vectors to guarantee convergence in the iterative process (Bagheri *et al.* 2009). Furthermore, determining this time interval necessitates supplementary frequency-domain analysis, such as power spectral density

https://doi.org/10.1017/jfm.2026.11934 Published online by Cambridge University Press

(*a*)

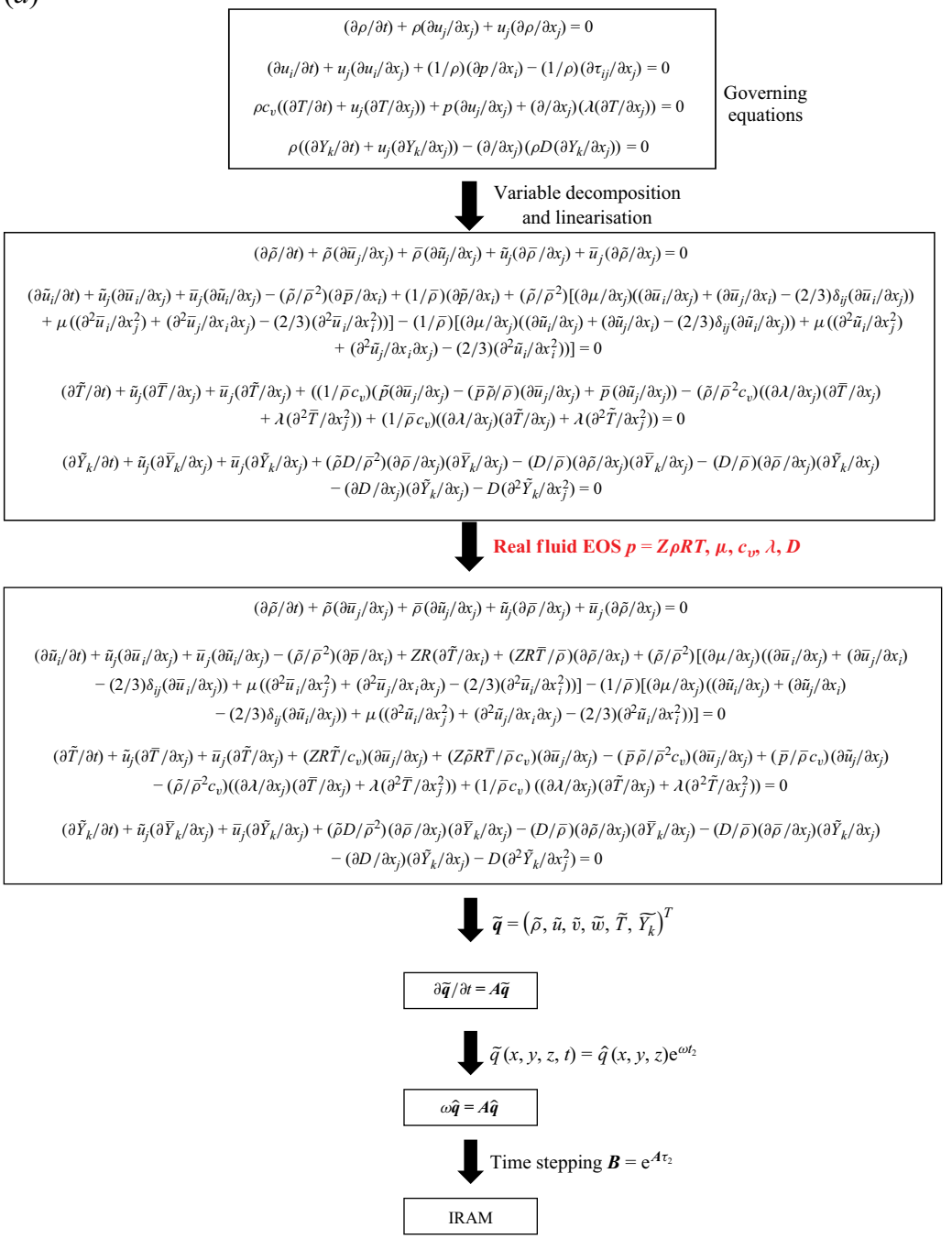


Figure 2. For caption see next page.

(PSD) analysis and the spectral analysis of proper orthogonal decomposition (POD) modal coefficients. More details about the time-stepper method can be found in Bagheri *et al.* (2009). The mean flows obtained from the numerical simulations in this study are employed as the base flow for GLSA.

https://doi.org/10.1017/jfm.2026.11934 Published online by Cambridge University Press

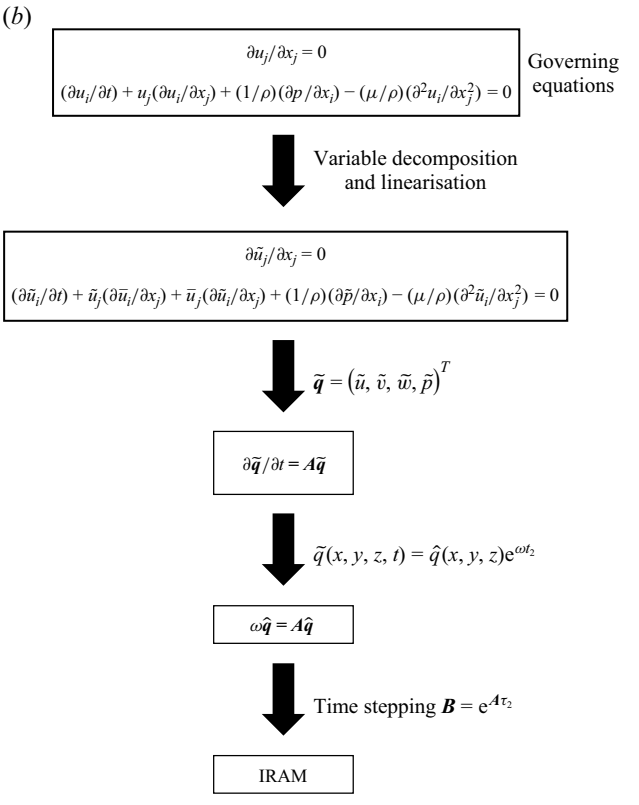


Figure 2 (cntd). Flowchart of GLSA algorithm for (*a*) real fluids and (*b*) incompressible fluids.

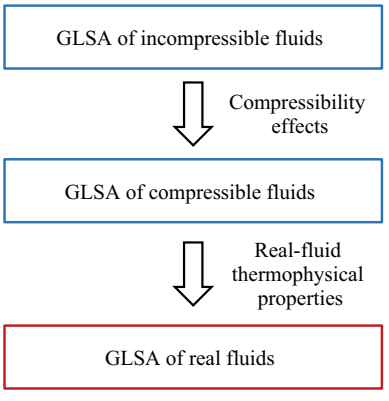


Figure 3. Schematic of GLSA classification.

As shown in Appendix A, matrix $\boldsymbol{A}$ is of dimension $6m \times 6m$ (m is the number of sampling grid points), while matrix $\boldsymbol{A}^*$ is of dimension $4m \times 4m$. Furthermore, each submatrix block of $\boldsymbol{A}$ contains a significantly greater number of components. Thus, the computational cost of the real-fluid algorithm is significantly higher than that of the incompressible-fluid algorithm. Taking the GLSA of a supercritical JICF in this study as an example, using a Dell high-performance workstation (a total of 40 CPUs, each with 2.1 GHz Intel Xeon Gold 5218R), the incompressible-fluid algorithm requires

https://doi.org/10.1017/jfm.2026.11934 Published online by Cambridge University Press

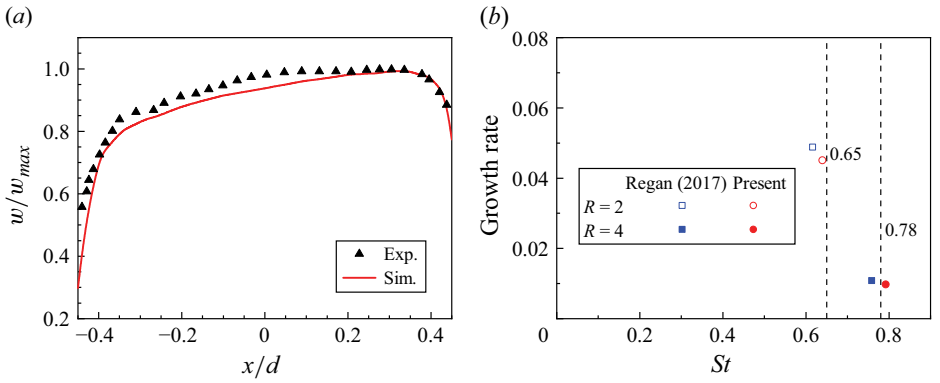


Figure 4. (*a*) Comparison of time-averaged transverse velocity profiles between experiment (Megerian *et al.* 2007) and present simulation, measured at $z/d = 0.1$ on the jet-centre plane ($Re_j = 2000$, $R = 2$). (*b*) Eigenvalue spectrum of GLSA for JICF obtained by Regan & Mahesh (2017) and present study.

approximately 20 minutes for matrix $\boldsymbol{A}$ construction and 4 minutes for eigenvalue decomposition, whereas the real-fluid algorithm takes around 100 minutes and 23 minutes for these operations, respectively.

2.3. *Validation*

To the authors' best knowledge, there are no publicly reported GLSA results that account for the real-fluid effects in trans/supercritical fluid flows. Consequently, the reliability of GLSA developed in this study is first validated against the GLSA results for incompressible, equidensity JICF reported by Regan & Mahesh (2017). The jet Reynolds number Re_j is 2000 ($R = 2$ and 4) with a nozzle exit diameter of 3.81 mm. The nozzle geometry is defined by a fifth-order polynomial. The parameter settings of IRAM are established based on the data provided in the literature. Figure 4(*a*) first compares the time-averaged transverse velocity profiles at the jet exit ($z/d = 0.1$ on the jet-centre plane) obtained from experiment (Megerian *et al.* 2007) and present numerical simulation under identical flow conditions ($Re_j = 2000$, $R = 2$). The results demonstrate good agreement, with an average relative deviation of 4.1 %, thereby confirming the reliability of the base flow employed in this study. Figure 4(*b*) illustrates the eigenvalue spectrum of GLSA, by comparing the results obtained by Regan & Mahesh (2017) with those from the present study. The eigenvalues have been non-dimensionalised, with the growth rate represented as $\omega_r d/(2\pi U_{j,max})$ and the Strouhal number as $\omega_i d/(2\pi U_{j,max})$. Good agreement is achieved at different velocity ratios. For cases with $R = 2$ and 4, the relative deviations in the magnitude of the eigenvalues are 3.8 % and 4.4 %, respectively. These results confirm the validity of the present GLSA algorithm.

To further validate the reliability of the proposed GLSA algorithm, a comparative analysis is conducted against the GLSA results of a compressible flow reported in the literature (Guiho *et al.* 2013). The flow of concern is a separated compressible boundary layer downstream of a bump. The free-stream Mach number is 0.1 and the Reynolds number, based on the inlet boundary layer displacement thickness δ^*, is 600. The bump height h is $2\delta^*$. The base flow is illustrated in figure 5, with density calculated using the compressible model. The reattachment point is located approximately at $x/\delta^* = 140$. Figure 6 compares the eigenvalues of the unstable eigenmodes derived from the literature with those computed by the proposed real-fluid GLSA algorithm. The eigenvalues are non-dimensionalised using the displacement thickness and the free-stream velocity. The results

https://doi.org/10.1017/jfm.2026.11934 Published online by Cambridge University Press

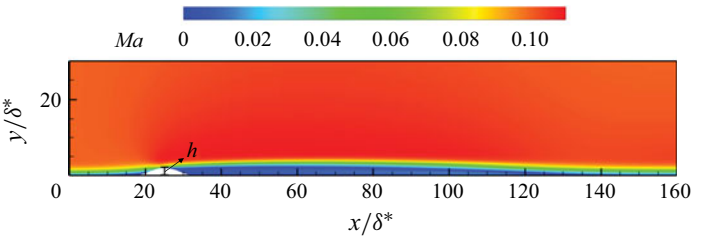


Figure 5. Mach number distribution of compressible base flow ($Ma = 0.1$, $Re = 600$, $h = 2\delta^*$).

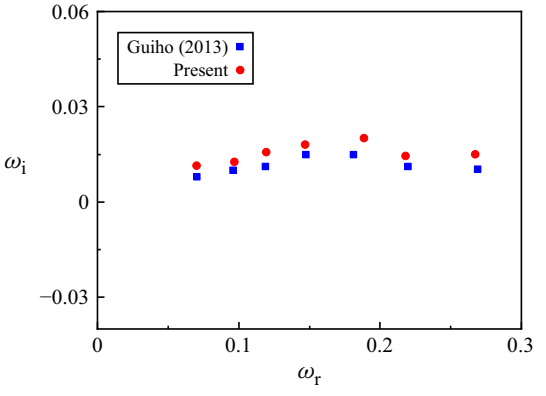


Figure 6. Eigenvalue spectrum of GLSA for flow behind a 2D bump, obtained by Guiho *et al.* (2013) and present study.

show close agreement with those of Guiho *et al.* (2013), with an average relative deviation of 1.2 % in the eigenvalue magnitudes. This consistency further supports the reliability of the proposed algorithm.

The following section introduces a case study of the supercritical JICF under different conditions to demonstrate the efficacy of the aforementioned GLSA algorithm in analysing the stability of supercritical fluid flows.

3. Case study of supercritical JICF

As mentioned earlier, JICF is a fundamental element for fuel–air mixing and film cooling in advanced propulsion systems. However, a JICF at supercritical pressure complicates the physical processes by introducing strong real-fluid effects. The developed GLSA framework can effectively analyse the stability characteristics of supercritical JICF. To this end, the physical problem under investigation is first delineated and the base-flow solution is briefly presented. Subsequently, the GLSA framework is utilised to systematically investigate the influence of momentum flux ratios and real-fluid effects on the flow stability of supercritical JICF, by deriving the eigenmodes and their corresponding growth rates for small perturbations across various cases. Additionally, as outlined in § 3.3, the aforementioned process further requires the application of techniques such as PSD and POD to determine the time interval τ involved in the time-stepper method.

https://doi.org/10.1017/jfm.2026.11934 Published online by Cambridge University Press

Case	$T_{j,r}$	$T_{c,r}$	p_r	R	S	J	Re_j
1	0.91	1.06	3.30	0.75	12.7	7.1	2000
2	0.91	1.06	1.65	0.75	23.4	13.2	2224
3	0.91	1.06	1.65	0.55	23.4	7.1	1631
A	2.17	2.17	0.03	2.66	1	7.1	1631

Table 1. Operating conditions.

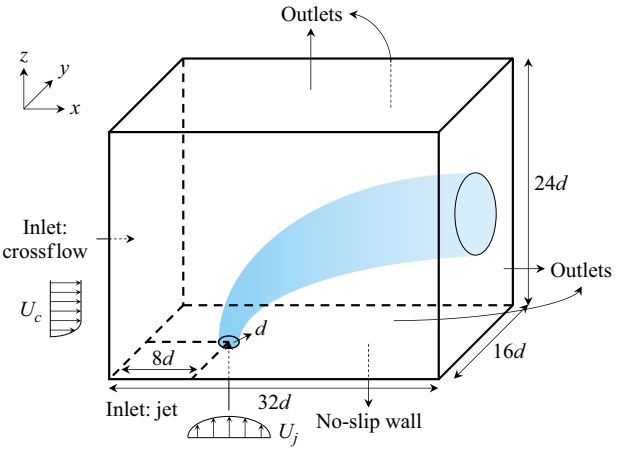


Figure 7. Schematic of computational domain.

3.1. *Problem description*

Figure 7 provides a schematic representation of the computational domain for the base flow, encompassing the regions defined by $-8 \leqslant x/d \leqslant 24$, $-8 \leqslant y/d \leqslant 8$ and $0 \leqslant z/d \leqslant 24$ in the streamwise, spanwise and transverse directions, respectively. The round jet orifice, with a diameter of $d = 0.5$ mm, is positioned at the origin of the domain. To facilitate the numerical set-up, N-dodecane is chosen as a surrogate of the fuel jet, while oxygen is utilised as the crossflow.

Table 1 summarises the operational parameters, including the jet-to-crossflow velocity ratio (R), density ratio (S) and momentum flux ratio (J) for the selected cases. The jet injection temperature (T_j), crossflow temperature (T_c) and ambient pressure (p_a) are non-dimensionalised with respect to the critical values of the jet:

$$T_{j,r} = \frac{T_j}{T_{cr,j}}, \tag{3.1}$$

$$T_{c,r} = \frac{T_c}{T_{cr,j}}, \tag{3.2}$$

$$p_r = \frac{p_a}{p_{cr,j}}. \tag{3.3}$$

The subscript 'r' denotes the reduced parameters. In cases 1–3 the jet is at supercritical pressures, whereas the crossflow may not necessarily be, as the ambient pressure in the simulated cases does not always exceed the critical pressure of oxygen. The jet Reynolds numbers (based on jet mean velocity U_j and d) in each case are set to approximately 2000.

https://doi.org/10.1017/jfm.2026.11934 Published online by Cambridge University Press

Case	Axial	Radial	Azimuthal
1	3.18–6.53	2.12–6.05	5.09–9.85
2	3.55–7.01	2.25–6.55	5.49–9.41
3	2.76–5.58	1.85–5.23	4.26–8.33
A	2.94–5.59	1.75–5.22	4.23–8.23

Table 2. Summary of grid sizes in intermediate grid system near the nozzle exit, normalised by the Kolmogorov scale.

A total number of four cases are conducted at various reduced pressures (p_r). Cases 1–3 operate at supercritical pressure ($p_r > 1$), while case A is at atmospheric pressure. Case A is configured with both the jet and crossflow composed of air ($J = 7.1$, Re_j identical to that of case 3) for comparison. The air density is computed using the compressible ideal-gas law, which will be discussed in detail in § 3.2.

Dynamic mesh adaptation is utilised to facilitate efficient and accurate grid refinement. To resolve the substantial density difference between jet and crossflow, as well as the abrupt density variations caused by temperature gradients within the mixing layer at supercritical pressures, localised mesh refinement is implemented in the vicinity of the jet plume and mixing layer. Additionally, a near-wall grid size of $y^+ = 1$ is maintained to ensure the accurate resolution of wall boundary layers. To achieve adequate numerical resolution, the grid system utilised in this study was validated via a grid independence study. Three distinct resolution levels were evaluated, with the grid size at the nozzle exit halved at each successive level. The time-averaged flow profile distributions demonstrated good consistency across all three levels. While the finest resolution level is capable of resolving small-scale eddies, the intermediate level is chosen to balance computational efficiency with numerical accuracy.

Table 2 presents a summary of the axial, radial and azimuthal grid sizes in the intermediate grid system near the nozzle exit, evaluated relative to the Kolmogorov scale, which is computed as

$$\eta \approx d \cdot Re_j^{-\frac{3}{4}}. \tag{3.4}$$

Evidently, the grid scales near the jet exit in both axial and radial directions approach the Kolmogorov scale. The final number of grid points after adaptive mesh refinement ranges between 31–38 million across different cases. The governing equations are discretised on a collocated grid. A uniform time step of 0.4 μs is adopted across all simulations to guarantee the acquisition of temporally precise data. The inlet flow at the jet orifice is characterised by a parabolic velocity profile. The bottom wall is subjected to no-slip and adiabatic boundary conditions. Undesirable wave reflections are minimised by applying non-reflecting boundary conditions at the downstream boundaries, achieved through the extrapolation of primitive variables from the interior domain.

3.2. *Base flow*

Numerical simulations of the base flows in different cases are performed using the theoretical foundation introduced in § 2.1. Figures 8 and 9 illustrate the instantaneous isosurfaces of Q-criterion at a value of 5×10^6 in cases 1–3 from different views, coloured by the jet mass fraction. Distinctive vortical structures are observed. Regions shaded in blue represent oxidiser-enriched mixtures originating from the crossflow, while red

https://doi.org/10.1017/jfm.2026.11934 Published online by Cambridge University Press

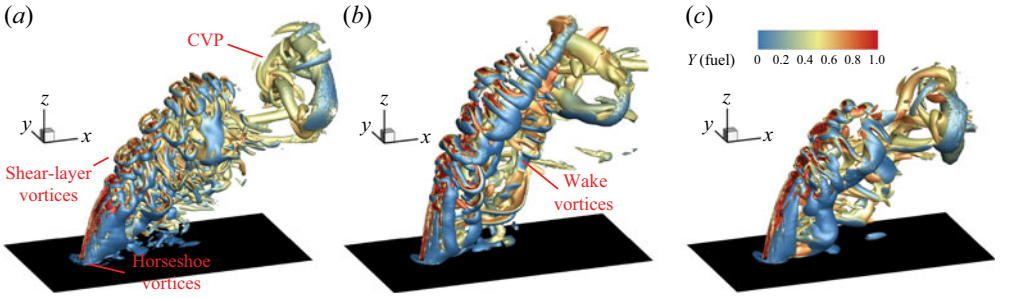


Figure 8. Instantaneous isosurfaces of $Q = 5 \times 10^6$ from an isometric view, coloured by the mass fraction of fuel: (*a*) case 1, (*b*) case 2, (*c*) case 3.

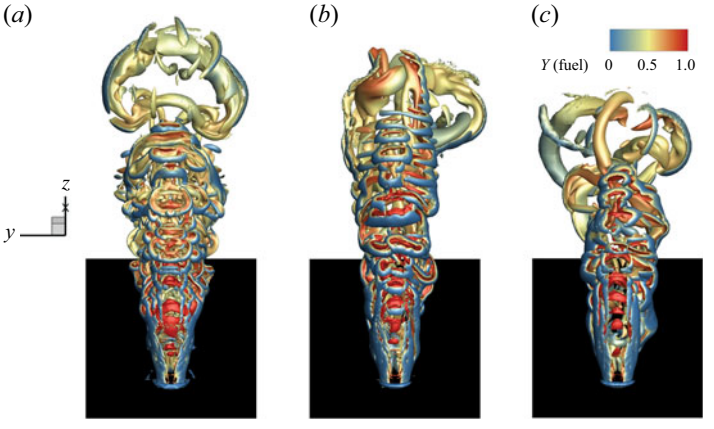


Figure 9. Instantaneous isosurfaces of $Q = 5 \times 10^6$ from a top view, coloured by the mass fraction of fuel: (*a*) case 1, (*b*) case 2, (*c*) case 3.

regions correspond to fuel-rich mixtures emanating from the jet. Shear-layer vortices, generated by a tangential velocity difference, are prominently observed on the windward side of the jet plume. These are followed by smaller-scale vortices, indicating a transitional or turbulent flow state. Notably, the smaller-scale vortices are more pronounced in case 1 ($p_r = 3.30$, $J = 7.1$). With the increase in J, the jet penetration depth in case 2 ($p_r = 1.65$, $J = 13.2$) is significantly enhanced, which facilitates deeper intrusion of the wake vortices in the transverse direction. Close to the wall, horseshoe vortices and small-scale vortices within the wake zone are observed. The latter are more evident in case 1, indicating a stronger interaction between the jet and the wall. Despite the same J as that of case 1, case 3 ($p_r = 1.65$, $J = 7.1$) exhibits large vortical structures due to the reduction in Re_j and the intensified density stratification in the jet's upstream region at a low supercritical pressure. The shear-layer vortices are diminished, while finger-like, large-scale wake vortices become apparent. These observations indicate that a reduction in ambient pressure induces significant alterations in the flow structures of supercritical JICF.

In the downstream region, a distinct symmetric CVP structure is observed in case 1. As illustrated in the top view of figure 9(*a*), the transient flow field exhibits near symmetry about the jet-centre plane, which is a characteristic feature of a globally unstable transverse jet (Karagozian 2014; Gevorkyan *et al.* 2016). In contrast, as shown in figures 9(*b*) and 9(*c*), the transient flow fields in cases 2 and 3 display asymmetry, indicative of convectively

https://doi.org/10.1017/jfm.2026.11934 Published online by Cambridge University Press

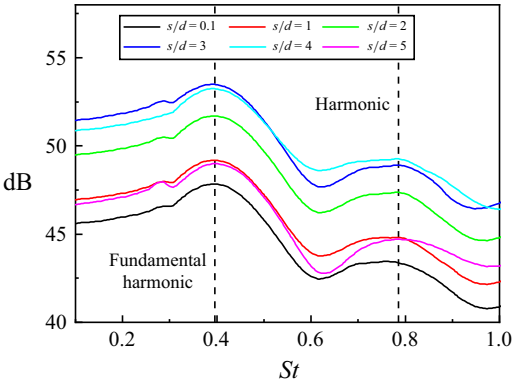


Figure 10. The PSD of transverse velocity fluctuations at various locations along the jet's USL (case A).

unstable transverse jets. This difference seems counter-intuitive since cases 1 and 3 have the same momentum flux ratio. In the following, we explain theoretically the fundamental mechanism underlying the instability characteristics using GLSA.

3.3. *Global linear stability analysis – momentum-flux-ratio effects*

Prior to examining the global stability of JICF at supercritical pressures, a discussion on the stability of a jet's USL in air JICF (case A) is first presented as a reference at atmospheric pressure. Power spectral density analysis of the base flow is utilised to identify the dominant frequency of flow-field disturbances, thereby facilitating an informed selection of the time interval τ. Velocity fluctuations are measured at multiple locations within the flow field. Figure 10 presents the PSD of transverse velocity (w) fluctuations recorded at various locations along the USL, expressed in terms of normalised coordinates (s/d, where s represents the distance along the time-averaged jet's upstream streamline that originates from $x/d, z/d = -0.5, 0$) on the jet-centre plane ($y/d = 0$). Power spectral density is expressed in dB ($S_{\mathrm{dB}}(w) = 10\log_{10}(S_{xx}(w))$, where $S_{xx}(w)$ denotes the PSD of w). Case A exhibits a dominant common tone instability along the USL, characterised by a Strouhal number ($St = fd/\overline{U_j}$) consistently maintained at approximately 0.4, which is indicative of global instability.

A global stability analysis is then conducted for case A. It is noteworthy that, as inferred from table 1, the mean jet velocity $\overline{U_j}$ is around 47.6 m/s. This results in a variable Mach number up to 0.30 in the flow field, implying that the compressibility effect in the flow is non-negligible and necessitating the use of the compressible ideal-gas law for density calculations. To demonstrate this, the two GLSA algorithms introduced in § 2.2 are carried out. In the real-fluid algorithm, matrix $\boldsymbol{A}$ is derived from (2.15), (2.18), (2.21) and (2.22), whereas in the incompressible-fluid algorithm, it is obtained from (2.27) and (2.28). It should be noted that the real-fluid algorithm employed in case A adopts the ideal-gas thermophysical properties to be consistent with the solver for the base flow. This differs slightly from the real-fluid algorithm applied later to JICF at supercritical pressures.

Figure 11 illustrates the most unstable eigenvalues ($St \approx 0.39$) derived from real-fluid and incompressible-fluid GLSA algorithms. For the incompressible-fluid algorithm, the instability growth rate is significantly higher, reaching the same order of magnitude as St. The maximum pressure fluctuation $(\Delta p/p)_{max}$ and density fluctuation $(\Delta\rho/\rho)_{max}$ in the flow field are 1.4 % and 1.2 %, respectively, indicating discernible compressible effects. Nonetheless, the incompressible-fluid algorithm leads to a nearly five-fold amplification of the growth rate compared with the real-fluid algorithm. This may seem unexpected, as

https://doi.org/10.1017/jfm.2026.11934 Published online by Cambridge University Press

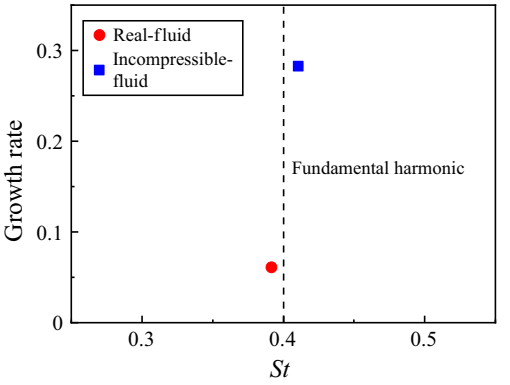


Figure 11. The GLSA eigenvalue spectrum obtained by real-fluid and incompressible-fluid algorithms for case A.

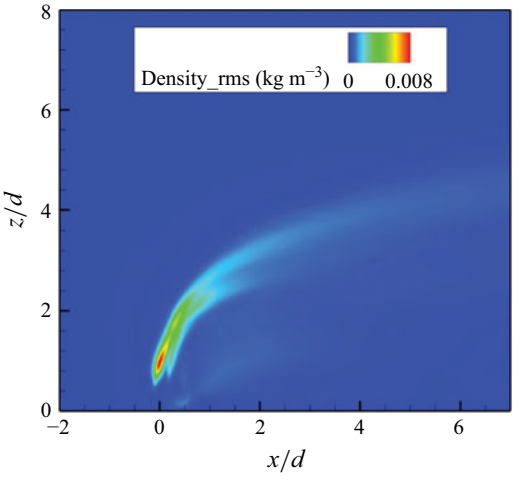


Figure 12. Root mean square (rms) contours of density on the jet-centre plane for case A.

GLSA applied to a mean flow usually yields eigenvalues characterised by minimal growth rates (Barkley 2006; Turton *et al.* 2015). Wan *et al.* (2025) showed that density variations introduce mean density-gradient effects, which tend to weaken the turbulent kinetic energy by damping turbulence production, thereby suppressing the development of flow instabilities. Since the real-fluid algorithm explicitly accounts for the spatial fluctuations of density in the flow field, as illustrated in figure 12, these stabilising effects can be captured in the stability analysis. Consequently, it predicts a low modal growth rate compared with the incompressible-fluid algorithm. The incompressible algorithm fails to incorporate a density fluctuation effect. Furthermore, as illustrated in figure 13(*a*), the eigenmode of $\tilde{w}$ obtained using the real-fluid algorithm exhibits a regular shape, indicative of disturbance propagation along the USL. In comparison, as shown in figure 13(*b*), the eigenmode from the incompressible-fluid algorithm displays additional small-scale structures, with discontinuous regions of alternating positive and negative values near $(x/d, z/d) = (0, 1)$. This discrepancy likely stems from the intrinsic incompatibility between the base flow $(\overline{u}, \overline{v}, \overline{w}, \overline{p})^{\mathrm{T}}$ extracted from the present compressible solver and the incompressible GLSA algorithm.

https://doi.org/10.1017/jfm.2026.11934 Published online by Cambridge University Press

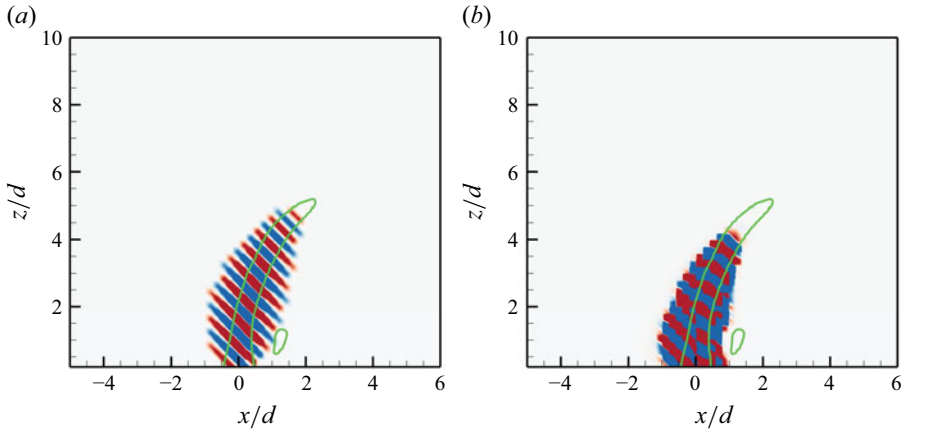


Figure 13. Real part of eigenmodes on the jet-centre plane, obtained by (*a*) real-fluid and (*b*) incompressible-fluid algorithms for case A (positive and negative lumps: isocontours of $\tilde{w}$; green lines: isolines of $\overline{w} = 20$ m/s).

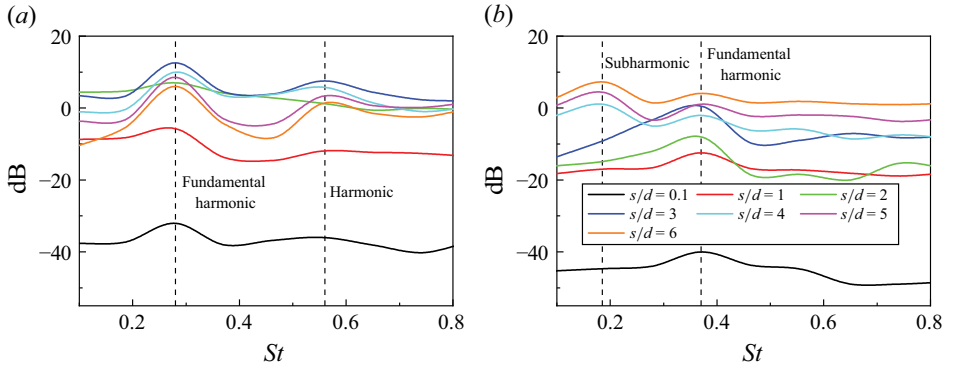


Figure 14. The PSD of transverse velocity fluctuations at various locations along the jet's USL: (*a*) case 1, (*b*) case 2.

Consequently, when compressible effects become non-negligible, the application of the incompressible-fluid algorithm to compressible base flows could introduce significant errors. Particularly, when the fluid properties of the base flow are evaluated using a real-fluid property framework, the incompressible-fluid algorithm leads to significantly larger errors. This underscores the necessity of utilising the real-fluid algorithm for GLSA implementation for real-fluid base flows, such as JICF at supercritical pressures in this study.

Subsequently, the real-fluid GLSA algorithm is leveraged to conduct a comprehensive stability analysis for cases 1–3. To investigate the impact of the momentum flux ratio on the stability characteristics of JICF at supercritical pressures, a comparative analysis between cases 1 and 2 is carried out. To appropriately determine the time interval τ for GLSA and to clarify the stability of the jet's USL, figure 14 displays the PSD of transverse velocity fluctuations of the base flow measured at multiple positions along the jet's USL in cases 1 and 2. A total of 12 500 snapshots were acquired at a time step of 0.4 μs. Based on the Nyquist–Shannon sampling theorem, this configuration yields a frequency resolution spanning the range of 2–1250 kHz. In case 1 ($p_r = 3.30$, $J = 7.1$),

https://doi.org/10.1017/jfm.2026.11934 Published online by Cambridge University Press

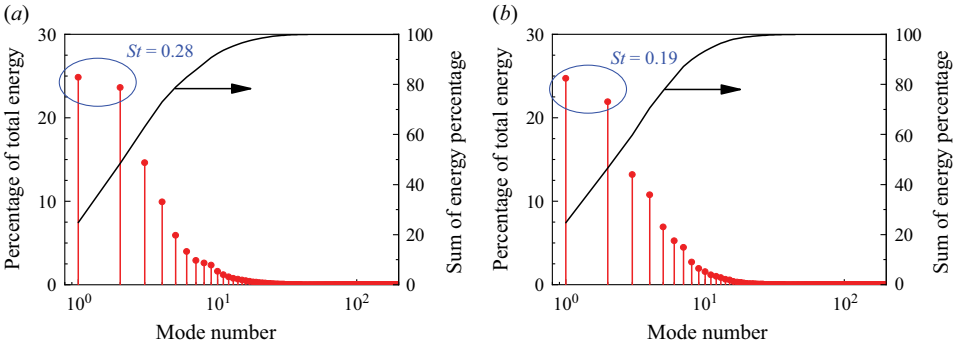


Figure 15. Energy distribution of POD modes for transverse velocity fluctuations in (*a*) case 1, (*b*) case 2.

a pure tone instability is evident throughout the shear layer, with a dominant Strouhal number consistently around 0.28. This behaviour signifies global instability and closely matches the characteristics observed in case A. In case 2 ($p_r = 1.65$), as J is increased to 13.2, the fundamental mode of JICF demonstrates a shift toward lower frequencies (from $St = 0.37$ to $St = 0.19$). When $s/d > 3$, the subharmonic mode becomes dominant, signalling the onset of convective instability. This transition in the dominant instability mode can be attributed to the variation in J, which is primarily driven by pressure-induced changes in fluid density. Note that the momentum flux ratios in cases 1 and 2 align with the empirical transition criterion distinguishing global and convective instability, where the critical momentum flux ratio is about 10 (Karagozian 2014; Getsinger *et al.* 2014; Shoji *et al.* 2020). Furthermore, the perturbation amplitudes at various locations of the USL in case 1 are larger than those in case 2, indicating a higher degree of flow instability in the former.

Given the identified shift of the dominant frequency in the jet's USL (case 2), POD is further employed to identify the dominant frequencies of the base flow-field variations across a large spatial domain, which is also useful to ascertain the suitable time interval τ in GLSA. For computational efficiency, the data extracted from the jet-centre plane is utilised, which allows for the effective extraction of flow characteristics associated with shear-layer vortices. The sampling frequency and time interval are maintained consistent with those in the PSD analysis. For a specified flow property, the POD analysis enables the projection of spatiotemporal fluctuations onto an optimal subspace spanning a set of orthogonal spatial functions (POD modes), which minimises the associated L2 error for reconstruction. Additional information on this methodology is available in Berkooz *et al.* (1993). Figure 15 presents the energy distribution of POD modes for transverse velocity fluctuations in cases 1 and 2, accompanied by the Strouhal numbers of the first two POD modes derived from the frequency spectra of their time-dependent coefficients. In case 1 the dominant POD modes correspond to the fundamental harmonic frequency ($St = 0.28$) identified in the PSD analysis, while the dominant POD modes are associated with the subharmonic frequency ($St = 0.19$) in case 2.

The GLSA based on the real-fluid algorithm is conducted following the aforementioned analyses. The 30 leading eigenvalues are computed with a maximum residual of 1×10^{-14}. Sixty Arnoldi vectors are generated during each iteration of the IRAM. In case 1, a Strouhal number of 0.28 corresponds to a period of 3.57 non-dimensional time units (normalised by d/U_j), with the time interval τ set to 1.4 time units, which is less than half of 3.57 time units. In case 2 the period increases to 5.26 time units at $St = 0.19$, with τ set to 2.2 time units, which is less than half of 5.26 time units. Notably, the nozzle

https://doi.org/10.1017/jfm.2026.11934 Published online by Cambridge University Press

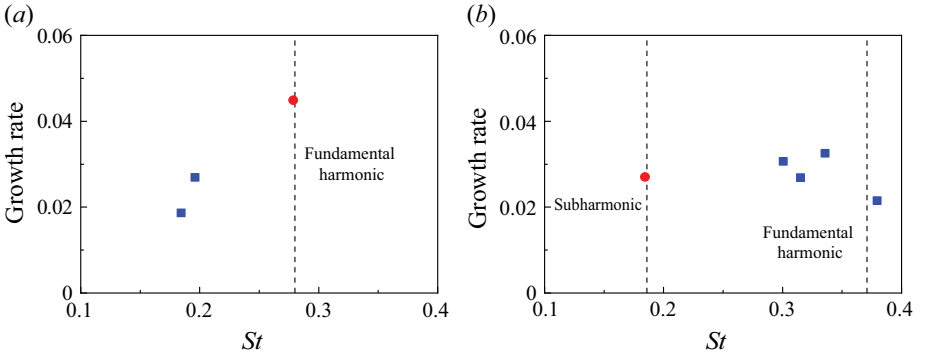


Figure 16. The GLSA eigenvalue spectrum for (*a*) case 1, (*b*) case 2.

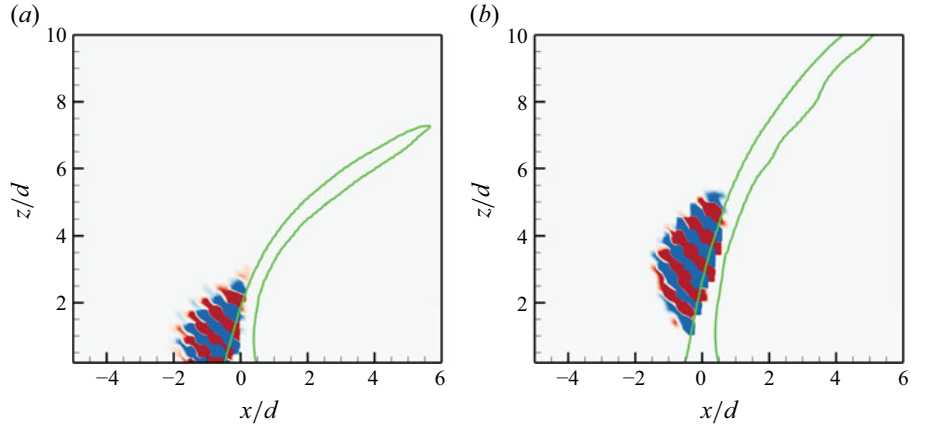


Figure 17. Real part of the eigenmodes on jthe et-centre plane: (*a*) case 1, $St = 0.28$; (*b*) case 2, $St = 0.19$ (positive and negative lumps: isocontours of $\tilde{w}$; green lines: isolines of $\overline{Y_1} = 0.7$).

diameter for fuel injection is typically small (0.5 mm in this study), resulting in a large scaling factor for τ compared with values reported in the literature (Bagheri *et al.* 2009; Regan & Mahesh 2017). Nevertheless, the selected time intervals still satisfy the Nyquist criterion.

Figure 16 presents the eigenvalue spectra derived from the GLSA calculations in cases 1 and 2, where the Strouhal numbers of the red dots coincide with the POD modes that exhibit the highest energy contribution. For each case, 100 Arnoldi vectors were solved per iteration within the IRAM. From the final results, a subset of eigenvalues that was selected for presentation exhibit both relatively large magnitudes among the 100 eigenvalues and distinctly different Strouhal numbers. In case 1 the eigenvalue at $St = 0.28$ dominates and exhibits a significantly higher growth rate than the eigenvalues in case 2, which further corroborates the presence of a higher degree of flow instability in case 1. As shown in figure 16(*b*), the eigenvalue at $St = 0.19$ demonstrates a higher growth rate than those associated with the fundamental harmonic frequency ($St = 0.37$) in case 2, indicating that the subharmonic mode exerts a more substantial influence on flow-field perturbations. This observation is consistent with the results obtained from the POD analysis.

Figure 17 illustrates the distribution of the eigenmodes corresponding to the two red dots in figure 16 on the jet-centre plane. The green lines represent the contour of the

https://doi.org/10.1017/jfm.2026.11934 Published online by Cambridge University Press

	Incompressible fluids	Supercritical real fluids
Location	Jet's potential core	Jet windward side
Morphology	Neat parallel stripes	Localised small-scale structures

Table 3. Differences in primary stability modes of JICF for incompressible fluids and supercritical real fluids.

time-average fuel mass fraction with a value of 0.7. The eigenmode at $St = 0.28$ in case 1, as depicted in figure 17(*a*), originates near the jet nozzle exit and represents the upstream shear-layer instability. In contrast, figure 17(*b*) reveals that the eigenmode at $St = 0.19$ in case 2 emerges farther downstream, away from the jet nozzle exit, and is associated with the downstream shear-layer instability. These results suggest that the flow-field disturbances of a globally unstable transverse jet (case 1) are primarily driven by the upstream shear-layer instability, whereas for a convectively unstable transverse jet (case 2), the downstream shear-layer instability dominates. This aligns with the findings of Regan & Mahesh (2017).

Interestingly, compared with the eigenmode of the atmospheric-pressure air JICF depicted in figure 13(*a*), the eigenmodes in figure 17 exhibit two distinct features (as summarised in table 3): (i) the eigenmodes mainly locate on the jet windward side, whereas the eigenmode of the atmospheric-pressure air JICF is intersected by the jet's potential core region; and (ii) the eigenmodes display localised small-scale structures. These may be due to the intense variations in thermophysical properties within the mixing layer on the jet windward side, which significantly amplify flow disturbances in this region. As documented in the literature (Unnikrishnan *et al.* 2021; Ding *et al.* 2024*a*), density variations of 1–3 orders of magnitude may occur within a spatial scale of several tens of micrometers in mixing layers involving transcritical or supercritical fluid flows.

The significance of viscosity-related terms for eigenvalues and eigenmodes solved by the GLSA are discussed. For the real-fluid mixing layers of interest in this study, the Reynolds numbers exceed $O(10^3)$. Previous studies (Okongo & Bellan 2003; Fedioun & Lardjane 2005; Wang *et al.* 2022) have suggested that, in linear stability analysis, the influence of viscosity and the associated diffusion terms is negligibly small. To clarify this in the present problem, we also derive a new real-fluid operator neglecting viscous terms, and compare the GLSA results of the two real-fluid operators using the base-flow data from cases 1 and 2. The results indicate that the eigenvalues and their corresponding eigenmodes exhibit only minor variations. Neglecting the diffusion terms leads to a slight increase in the growth rate due to the removal of the viscous dissipation effect. Further details are provided in Appendix B. Additionally, to enable a more detailed quantitative comparison, the time-averaged and fluctuating components of the convection and diffusion terms in the momentum equation are used as examples for comparison. Note that although current GLSA results suggest the influence of viscous and diffusive terms is marginal, this study employs a JICF at a Reynolds number of approximately 2000 solely as a demonstrative case for the proposed GLSA algorithm. When addressing other supercritical fluid flows, particularly those characterised by lower Reynolds numbers and significant viscous effects, omitting viscous and diffusive terms would not be advised.

The subsequent discussion is grounded in vortex dynamics to elucidate the physical mechanisms underlying the GLSA results. The analyses presented in this section demonstrate that, under identical jet-to-crossflow velocity ratios, the stability of the JICF undergoes significant variations due to density changes induced by variations in ambient pressure. At high supercritical pressure (case 1, $J = 7.1$), the flow-field disturbances

https://doi.org/10.1017/jfm.2026.11934 Published online by Cambridge University Press

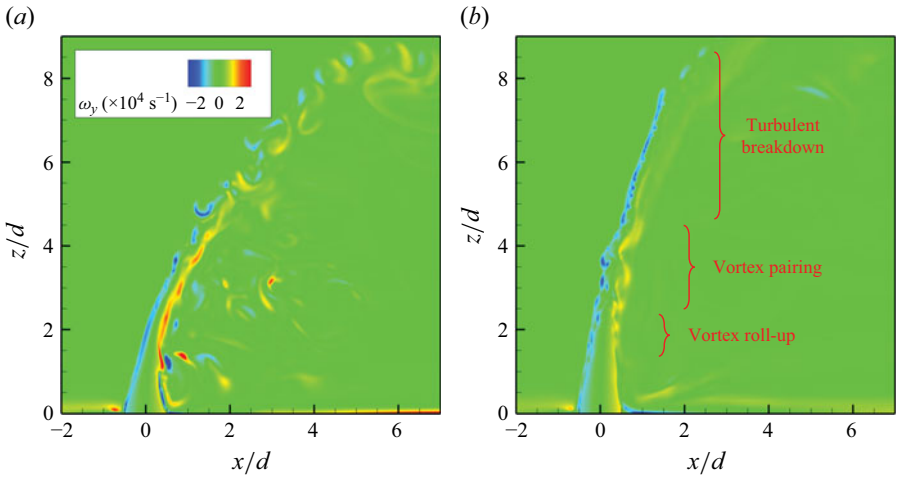


Figure 18. Instantaneous contours of y vorticity on the jet-centre plane: (a) case 1, (b) case 2.

are governed by the upstream fundamental harmonic instability. In contrast, at low supercritical pressure (case 2, $J = 13.2$), the downstream subharmonic instability becomes the dominant factor influencing the flow-field disturbances. The underlying mechanisms will be further investigated in the subsequent discussion. As illustrated in figure 14(a), the perturbation amplitude in case 1 reaches its maximum near $s/d = 3$, followed by a slight attenuation. This indicates that the perturbation energy is predominantly concentrated in the jet's upstream region. In the downstream region, higher harmonics emerge due to vortex breakdown, whereas subharmonics are scarcely observed. Therefore, the energy transfer from the fundamental harmonic to subharmonics is suppressed, which aligns with the characteristics of global instability (Strykowski & Niccum 1992). Conversely, in case 2 (figure 14b), the perturbation amplitude exhibits a gradual amplification along the jet's upstream streamline, indicating a progressive transfer of energy toward the downstream region. The emergence of subharmonics in the downstream area suggests the occurrence of vortex pairing. This represents energy transfer from smaller to larger scales, which is the characteristic of convective instability (Megerian *et al.* 2007; Getsinger *et al.* 2012).

The investigation into the causes of the aforementioned phenomena requires an analysis of the vorticity dynamics in the y direction, as shown in figure 18. Due to the high axial velocity of the jet compared with the crossflow, the shear-layer vortices on the jet windward and leeward sides exhibit counterclockwise and clockwise patterns on the jet-centre plane, respectively. These opposing rotational directions are visualised on the contours as distinct blue and red/yellow regions. Along the jet streamline, the shear layer can be categorised into three zones: vortex roll-up, vortex pairing and turbulent breakdown (Chandh *et al.* 2025). In case 1 (figure 18a), the vortices maintain relatively high intensity near the jet nozzle exit, and the spacing between adjacent vortex cores downstream is relatively large, which inhibits vortex pairing. However, in case 2 (figure 18b), the vortex intensity near the nozzle exit is weaker. Clear vortex cores begin to emerge at $z/d \approx 2$, and the close spacing between adjacent vortex cores facilitates vortex pairing. The vortex size exhibits a noticeable increase across the range of $2 < z/d < 4$. This can be attributed to velocity fluctuations of the vortices, which may cause trailing vortices to catch up with leading vortices (Zong & Yang 2007). As a result, the power spectrum exhibits a distinct subharmonic, accompanied by a shift in dominant frequency, until the vortices eventually break down into a fully turbulent shear layer.

https://doi.org/10.1017/jfm.2026.11934 Published online by Cambridge University Press

The observed variation in transient vorticity is directly linked to the inherent instabilities within the mixing layer. Given the identical velocity ratio R, the propagation velocities of vortices in the jet's upstream regions in cases 1 and 2 are expected to be comparable. Consequently, the spacing between adjacent vortex cores is influenced by the periodicity of vortex generation. This implies that the vortex generation frequency in the jet's upstream region of case 2 is higher than that of case 1, which aligns with the data presented in figure 14. Specifically, the Strouhal number of the fundamental harmonic is 0.28 in case 1, whereas it is 0.37 in case 2. Despite the similar shear strengths, which suggest equivalent influences of the Kelvin–Helmholtz instability in these two cases, the observed difference in vortex generation frequencies implies the involvement of additional contributing factors. Notably, as indicated in table 1, the density ratio (S) in case 2 is nearly twice that of case 1. This significant disparity raises the necessity of investigating the potential role of Rayleigh–Taylor (R-T) instability in modulating the vortex generation dynamics (Roberts & Jacobs 2015; Li & Soteriou 2018).

Subsequently, a more quantitative investigation of vortex dynamics is presented, and its connection to GLSA is elucidated. The quantification of vortex dynamics can be effectively accomplished through the application of the transport equation presented as

$$\frac{D\boldsymbol{\omega}}{Dt} = (\boldsymbol{\omega}\cdot\boldsymbol{\nabla})\boldsymbol{u} - (\boldsymbol{\nabla}\cdot\boldsymbol{u})\boldsymbol{\omega} - \boldsymbol{\nabla}\left(\frac{1}{\rho}\right)\times\boldsymbol{\nabla}p + \boldsymbol{\nabla}\times\left(\frac{1}{\rho}\boldsymbol{\nabla}\cdot\boldsymbol{\eta}\right), \tag{3.5}$$

where $\boldsymbol{\omega}$ denotes the vorticity vector and $\boldsymbol{\eta}$ represents the viscous stress tensor. On the right-hand side of the equation, the first term, vortex stretching, and the third term, baroclinic torque, serve as quantitative measures for characterising the magnitudes of the Kelvin–Helmholtz instability and the R–T instability, respectively.

Figure 19 illustrates the spatial distributions of the time-averaged vorticity transport budgets in the y direction in case 1 (left) and case 2 (right), normalised by the bulk velocity u_j and momentum thickness θ_0 at the nozzle exit. The baroclinic torque predominantly exerts its influence within the mixing layer regions. In both cases, given that the jet-to-crossflow density ratio S exceeds 10, the baroclinic torque demonstrates significantly greater intensity in the mixing layer regions than vortex stretching. In contrast, vortex stretching prevails in the lower wake region, where intense boundary layer separation and recirculation flow occur. Compared with case 1, the elevated density ratio S in case 2 significantly amplifies the dominance of baroclinic torque. This enhancement leads to a significant expansion of its influence regions, both upstream and downstream of the jet. Consequently, the enhanced R-T instability drives an increase in the frequency of the fundamental harmonic. Particularly, under the impact of the R-T instability, a distinct region of alternating positive and negative baroclinic torque is observed in the jet's downstream mixing layer ($3 < z/d < 6$) in case 2. This arises due to the formation of multiple CVPs. Furthermore, this region corresponds to the area where the GLSA eigenmode is located, as illustrated in figure 17(b).

Unlike case 1, a subharmonic emerges in the jet's downstream region in case 2. This phenomenon appears to result from the momentum flux ratio J exceeding the critical value of 10. However, the present GLSA results reveal that the underlying cause of this transition is attributed to the decrease in ambient pressure, which enlarges the density ratio S. The analyses of vortex dynamics further corroborate that this change amplifies the R-T instability, leading to the formation of a subharmonic in the jet downstream region. This mechanism distinctly differs from that reported in the literature, where subharmonics are induced by enhancing the K-H instability through an increase in the velocity ratio R (Megerian *et al.* 2007; Iyer & Mahesh 2016).

https://doi.org/10.1017/jfm.2026.11934 Published online by Cambridge University Press

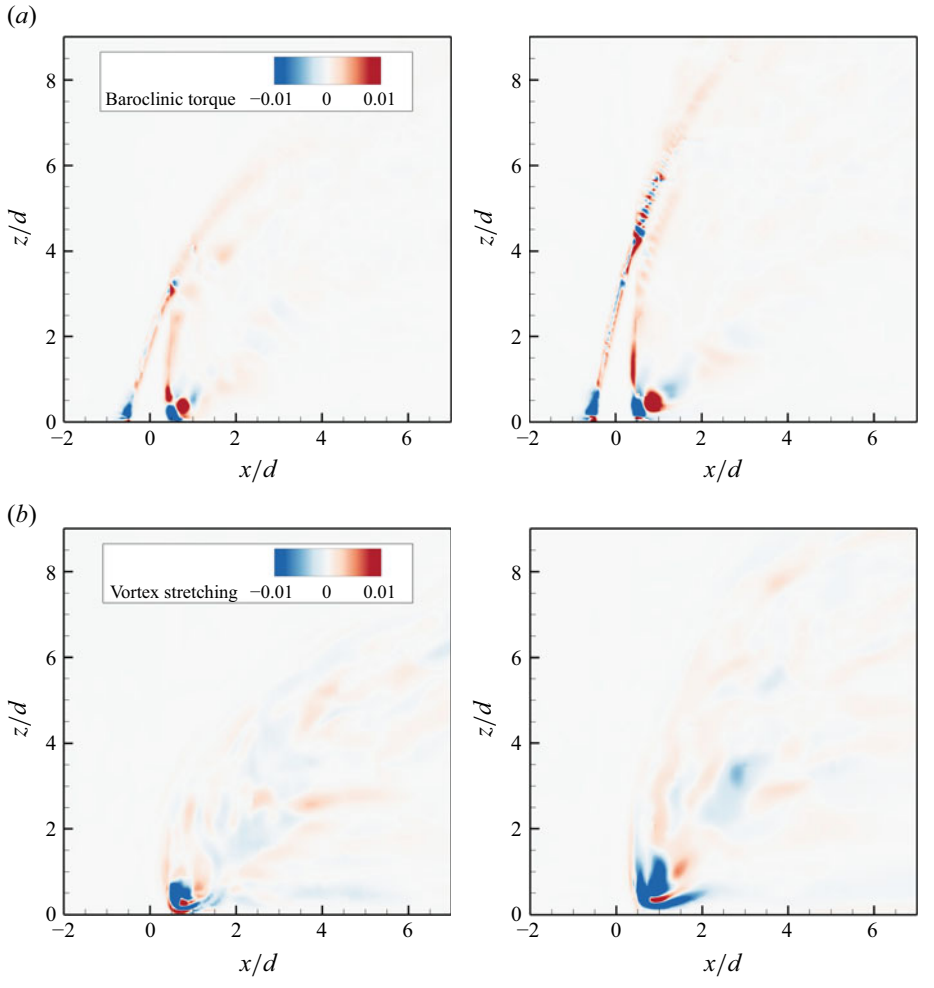


Figure 19. Spatial distributions of time-averaged vortex transport budgets in the y direction of case 1 (left) and case 2 (right), normalised by bulk velocity and momentum thickness at the nozzle exit $(\overline{u_j}/\theta_0)^2$: (*a*) baroclinic torque, (*b*) vortex stretching.

3.4. *Global linear stability analysis – real-fluid effects*

As discussed in § 3.2, the intensified real-fluid effects at a low supercritical pressure ($p_r = 1.65$), which results from pronounced density stratification, exerts a significant influence on the dynamics of supercritical JICF. To further explore the stability characteristics at low supercritical pressure, case 3 is established by reducing J from 13.2 to 7.1 (according to case 1).

As discussed in the previous section, the time interval τ in case 3 for GLSA is first determined. Figure 20(*a*) illustrates that in case 3, the characteristic frequency of the perturbations along the jet's upstream streamline undergoes a noticeable shift, mimicking the characteristics of a convective instability. The Strouhal number of the fundamental harmonic is 0.25, which is consistent with the first two POD modes in figure 20(*b*). At $s/d = 4$, the flow is in a transitional state, while at $s/d = 5$ and 6, the dominant frequency shifts to higher harmonics. Compared with case 1 in figure 14(*a*), the perturbation amplitudes in figure 20(*a*) are reduced. Additionally, the perturbation

https://doi.org/10.1017/jfm.2026.11934 Published online by Cambridge University Press

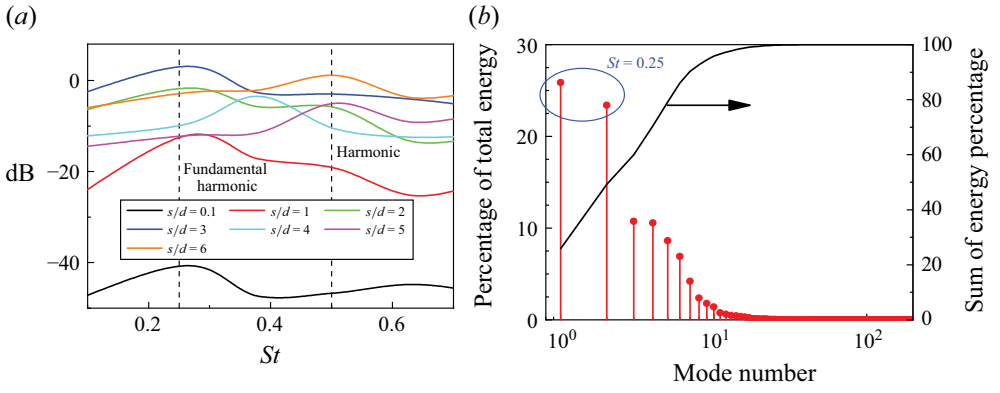


Figure 20. Stability analysis of case 3: (*a*) PSD of transverse velocity fluctuations at various locations along the jet's USL, (*b*) energy distribution of POD modes for transverse velocity fluctuations.

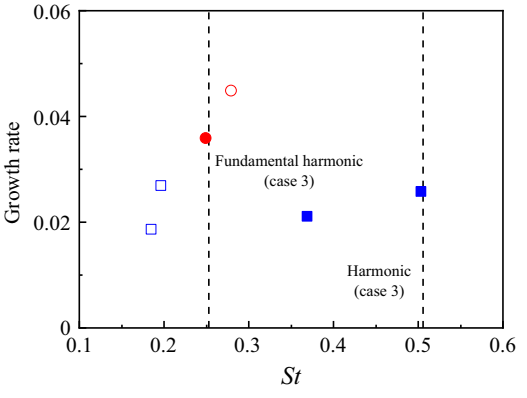


Figure 21. The GLSA eigenvalue spectrum for cases 1 (hollow symbols) and 3 (solid symbols).

amplitude generally amplifies along the jet's upstream streamline, although a slight decrease is observed during frequency shifting. This suggests that energy is gradually transferred downstream. However, unlike the convectively unstable JICF observed in case 2 and at subcritical pressures (Megerian *et al.* 2007; Getsinger *et al.* 2014), no subharmonic emerges downstream. Instead, the dominant frequency progressively shifts to higher harmonics that are generated due to vortex breakdown downstream, implying that energy is transferred to smaller scales. This phenomenon can be attributed to the reduced velocity difference in the shear layer due to the decreased jet velocity in comparison to case 2, which results in a lower vortex generation frequency and an extended spacing between adjacent vortex cores. Additionally, the pronounced density stratification also suppresses vortex pairing (Zong *et al.* 2004), making the formation of subharmonics more unlikely.

The GLSA eigenvalue spectrum for case 3 is presented in figure 21. In case 3, $St = 0.25$ corresponds to a period of 4, with τ set to 1.7 time units. Compared with the GLSA eigenvalues observed in case 1 (figure 16*a*), those in case 3 manifest diminished growth rates, which provide quantitative evidence that the enhanced real-fluid effects induced by pronounced density stratification stabilise the USL of the transverse jet at decreased supercritical pressure. This stabilisation may lead to an anomalous transition in the stability. Figure 22 depicts the spatial distribution of the eigenmodes in case 3 on the

https://doi.org/10.1017/jfm.2026.11934 Published online by Cambridge University Press

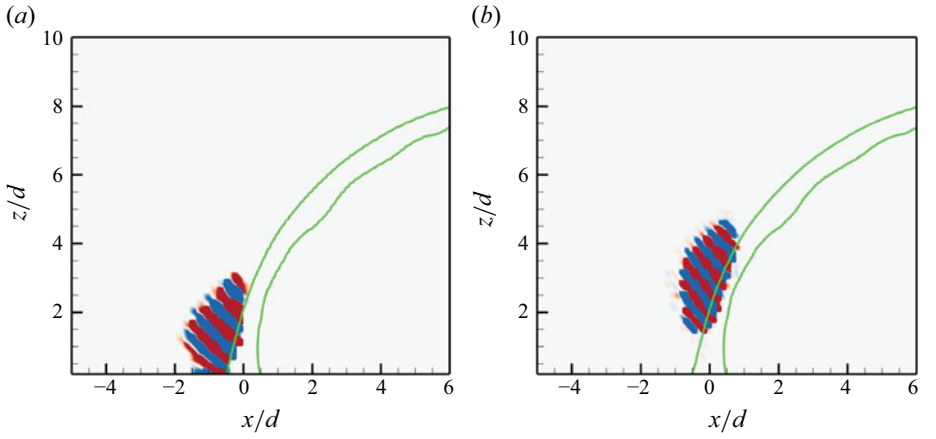


Figure 22. Real part of the eigenmodes on the jet-centre plane for case 3: (*a*) $St = 0.25$, (*b*) $St = 0.50$ (positive and negative lumps: isocontours of $\tilde{w}$; green lines: isolines of $\tilde{Y}_1 = 0.7$).

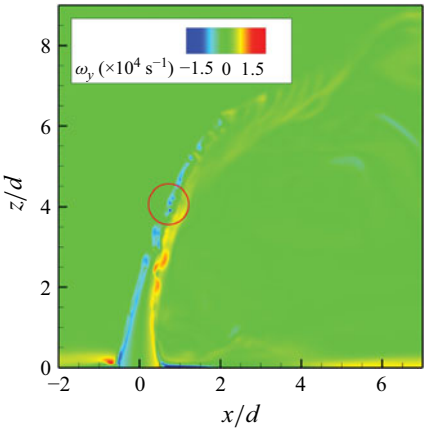


Figure 23. Instantaneous contours of the y vorticity on the jet-centre plane for case 3.

jet-centre plane. The eigenmode corresponding to $St = 0.25$ originates in close proximity to the nozzle exit, characterising the upstream shear-layer instability. Meanwhile, the eigenmode associated with $St = 0.50$ emerges further downstream with a shorter wavelength and represents a downstream shear-layer instability.

The results of GLSA are further elucidated through vortex dynamics. Figure 23 presents the instantaneous contour of y vorticity on the jet-centre plane in case 3. Compared with cases 1 and 2 (figure 18), the weak vortex intensity in the flow field necessitates a narrow colourbar range to clearly visualise the vorticity. As indicated by the red circle, vortex breakdown occurs at $z/d \approx 4$, leading to a frequency shift shown in figure 20(*a*). Its location coincides with the eigenmode identified in figure 22(*b*). In comparison to case 1, while the momentum flux ratio J remains identical, the density ratio S in case 3 increases, resulting in an enhanced R-T instability. However, the reduced velocity difference weakens the K-H instability within the shear layer. Consequently, under the coupled influence of these two factors, the Strouhal numbers of the fundamental harmonic in both cases are similar, with $St = 0.28$ in case 1 and $St = 0.25$ in case 3.

https://doi.org/10.1017/jfm.2026.11934 Published online by Cambridge University Press

4. Conclusion

The GLSA framework capable of incorporating real-fluid effects in supercritical fluid flows is proposed for the first time. It accounts for real-fluid effects via a cubic EOS and the detailed treatment of real-fluid thermodynamic and transport properties. Furthermore, it incorporates the energy and species transport equations within a unified set of linearised governing equations. As a representative example, the GLSA framework is employed to systematically investigate the stability characteristics of jets in crossflow at supercritical pressures. The base flows in GLSA are obtained through a unified numerical framework for real-fluid flow dynamics. By integrating the implicitly restarted Arnoldi iteration method with a time-stepper approach, this study elucidates the instability dynamics at jet Reynolds numbers of around 2000, with comparative insights drawn from an atmospheric-pressure air JICF case.

The results highlight that adopting an incompressible-fluid algorithm for compressible base flows yields anomalously increased growth rates, particularly when real-fluid effects are consequential. The GLSA framework successfully resolves the complex USL instabilities, with Strouhal numbers aligning closely with PSD analyses and POD results. It permits a more quantitative stability assessment and allows for the intuitive visualisation of eigenmodes. With a same jet-to-crossflow velocity ratio of 0.75, a decrease in ambient pressure can induce the transition of the eigenmode from originating near the nozzle exit to emerging farther downstream, while exhibiting a substantial decrease in growth rate magnitude. This corresponds to a shift of the USL from global to convective instability. The vorticity transport budget analysis demonstrates that this pressure reduction also amplifies R-T instabilities in the mixing layer. This mechanism facilitates downstream vortex pairing, promoting subharmonic formation. These observations underscore the significance of reduced pressure (p_r) as an additional governing parameter at supercritical pressures, except for the jet-to-crossflow momentum flux ratio (J), as it arises from the intensified real-fluid effects driven by pronounced density stratification near the critical pressure. Moreover, in this case ($J = 7.1$, $p_r = 1.65$), subharmonics are not observed in the jet's downstream region, which could be due to the reduced velocity difference in the shear layer, along with the significant density stratification that inhibits vortex pairing.

The novel real-fluid GLSA framework is extendable to stability analyses of various supercritical fluid flows. Given the continuous progression toward elevated operational pressures in propulsion and power-generation systems, this research offers a solid theoretical and technical foundation for advanced combustor design.

Acknowledgements. The authors thank Dr Dongjun Ma and Dr Chuhan Wang for their advice on linear stability analysis.

Funding. This work was sponsored by the National Natural Science Foundation of China (52276123).

Declaration of interests. The authors report no conflict of interest.

Appendix A. Linear operator $\boldsymbol{A}$

As mentioned in § 2.2, for the real-fluid algorithm, $\tilde{\boldsymbol{q}} = (\tilde{\rho}, \tilde{u}, \tilde{v}, \tilde{w}, \tilde{T}, \tilde{Y}_1)^{\mathrm{T}}$. Transforming equations (2.15), (2.18), (2.21, and (2.22) into the form of (2.23) yields the complete expression for $\boldsymbol{A}$, which is a matrix of size $6m \times 6m$, where m denotes the number of sampling grid points. The columns of the matrix are structured as follows (for simplicity,

https://doi.org/10.1017/jfm.2026.11934 Published online by Cambridge University Press

the overbar symbols of $\overline{\mu}$, $\overline{Z}$, $\overline{R}$, $\overline{c_v}$, $\overline{\lambda}$ and $\overline{D}$ have been omitted):

$$\begin{pmatrix} A_{\rho\rho} \\ A_{u\rho} \\ A_{v\rho} \\ A_{w\rho} \\ A_{T\rho} \\ A_{Y_1\rho} \end{pmatrix} = \begin{pmatrix} \dfrac{\partial \overline{u}}{\partial x} + \dfrac{\partial \overline{v}}{\partial y} + \dfrac{\partial \overline{w}}{\partial z} + \overline{u}\dfrac{\partial}{\partial x} + \overline{v}\dfrac{\partial}{\partial y} + \overline{w}\dfrac{\partial}{\partial z} \\ -\dfrac{1}{\overline{\rho}^2}\dfrac{\partial \overline{p}}{\partial x} + \dfrac{Z\overline{R}\,\overline{T}}{\overline{\rho}}\dfrac{\partial}{\partial x} + \dfrac{1}{\overline{\rho}^2}\left(\dfrac{4}{3}\dfrac{\partial \mu}{\partial x}\dfrac{\partial \overline{u}}{\partial x} + \dfrac{\partial \mu}{\partial y}\dfrac{\partial \overline{u}}{\partial y} + \dfrac{\partial \mu}{\partial y}\dfrac{\partial \overline{v}}{\partial x} + \dfrac{\partial \mu}{\partial z}\dfrac{\partial \overline{u}}{\partial z} + \dfrac{\partial \mu}{\partial z}\dfrac{\partial \overline{w}}{\partial x}\right) + \dfrac{\mu}{\overline{\rho}^2}\left(\dfrac{4}{3}\dfrac{\partial^2 \overline{u}}{\partial x^2} + \dfrac{\partial^2 \overline{u}}{\partial y^2} + \dfrac{\partial^2 \overline{v}}{\partial x \partial y} + \dfrac{\partial^2 \overline{u}}{\partial z^2} + \dfrac{\partial^2 \overline{w}}{\partial x \partial z}\right) \\ -\dfrac{1}{\overline{\rho}^2}\dfrac{\partial \overline{p}}{\partial y} + \dfrac{Z\overline{R}\,\overline{T}}{\overline{\rho}}\dfrac{\partial}{\partial y} + \dfrac{1}{\overline{\rho}^2}\left(\dfrac{\partial \mu}{\partial x}\dfrac{\partial \overline{v}}{\partial x} + \dfrac{\partial \mu}{\partial x}\dfrac{\partial \overline{u}}{\partial y} + \dfrac{4}{3}\dfrac{\partial \mu}{\partial y}\dfrac{\partial \overline{v}}{\partial y} + \dfrac{\partial \mu}{\partial z}\dfrac{\partial \overline{v}}{\partial z} + \dfrac{\partial \mu}{\partial z}\dfrac{\partial \overline{w}}{\partial y}\right) + \dfrac{\mu}{\overline{\rho}^2}\left(\dfrac{\partial^2 \overline{v}}{\partial x^2} + \dfrac{\partial^2 \overline{u}}{\partial y \partial x} + \dfrac{4}{3}\dfrac{\partial^2 \overline{v}}{\partial y^2} + \dfrac{\partial^2 \overline{v}}{\partial z^2} + \dfrac{\partial^2 \overline{w}}{\partial y \partial z}\right) \\ -\dfrac{1}{\overline{\rho}^2}\dfrac{\partial \overline{p}}{\partial z} + \dfrac{Z\overline{R}\,\overline{T}}{\overline{\rho}}\dfrac{\partial}{\partial z} + \dfrac{1}{\overline{\rho}^2}\left(\dfrac{\partial \mu}{\partial x}\dfrac{\partial \overline{w}}{\partial x} + \dfrac{\partial \mu}{\partial x}\dfrac{\partial \overline{u}}{\partial z} + \dfrac{\partial \mu}{\partial y}\dfrac{\partial \overline{w}}{\partial y} + \dfrac{\partial \mu}{\partial y}\dfrac{\partial \overline{v}}{\partial z} + \dfrac{4}{3}\dfrac{\partial \mu}{\partial z}\dfrac{\partial \overline{w}}{\partial z}\right) + \dfrac{\mu}{\overline{\rho}^2}\left(\dfrac{\partial^2 \overline{w}}{\partial x^2} + \dfrac{\partial^2 \overline{u}}{\partial z \partial x} + \dfrac{\partial^2 \overline{w}}{\partial y^2} + \dfrac{\partial^2 \overline{v}}{\partial z \partial y} + \dfrac{4}{3}\dfrac{\partial^2 \overline{w}}{\partial z^2}\right) \\ \left(\dfrac{Z\overline{R}\,\overline{T}}{\overline{\rho}c_v} - \dfrac{\overline{p}}{\overline{\rho}^2 c_v}\right)\left(\dfrac{\partial \overline{u}}{\partial x} + \dfrac{\partial \overline{v}}{\partial y} + \dfrac{\partial \overline{w}}{\partial z}\right) - \dfrac{\lambda}{\overline{\rho}^2 c_v}\left(\dfrac{\partial^2 \overline{T}}{\partial x^2} + \dfrac{\partial^2 \overline{T}}{\partial y^2} + \dfrac{\partial^2 \overline{T}}{\partial z^2}\right) - \dfrac{1}{\overline{\rho}^2 c_v}\left(\dfrac{\partial \lambda}{\partial x}\dfrac{\partial \overline{T}}{\partial x} + \dfrac{\partial \lambda}{\partial y}\dfrac{\partial \overline{T}}{\partial y} + \dfrac{\partial \lambda}{\partial z}\dfrac{\partial \overline{T}}{\partial z}\right) \\ \dfrac{D}{\overline{\rho}^2}\left(\dfrac{\partial \overline{\rho}}{\partial x}\dfrac{\partial \overline{Y_1}}{\partial x} + \dfrac{\partial \overline{\rho}}{\partial y}\dfrac{\partial \overline{Y_1}}{\partial y} + \dfrac{\partial \overline{\rho}}{\partial z}\dfrac{\partial \overline{Y_1}}{\partial z}\right) - \dfrac{D}{\overline{\rho}}\left(\dfrac{\partial}{\partial x}\dfrac{\partial \overline{Y_1}}{\partial x} + \dfrac{\partial}{\partial y}\dfrac{\partial \overline{Y_1}}{\partial y} + \dfrac{\partial}{\partial z}\dfrac{\partial \overline{Y_1}}{\partial z}\right) \end{pmatrix}, \tag{A1}$$

$$\begin{pmatrix} A_{\rho u} \\ A_{uu} \\ A_{vu} \\ A_{wu} \\ A_{Tu} \\ A_{Y_1 u} \end{pmatrix} = \begin{pmatrix} \overline{\rho}\dfrac{\partial}{\partial x} + \dfrac{\partial \overline{\rho}}{\partial x} \\ \dfrac{\partial \overline{u}}{\partial x} + \overline{u}\dfrac{\partial}{\partial x} + \overline{v}\dfrac{\partial}{\partial y} + \overline{w}\dfrac{\partial}{\partial z} - \dfrac{\mu}{\overline{\rho}}\left(\dfrac{4}{3}\dfrac{\partial^2}{\partial x^2} + \dfrac{\partial^2}{\partial y^2} + \dfrac{\partial^2}{\partial z^2}\right) - \dfrac{4}{3\overline{\rho}}\dfrac{\partial \mu}{\partial x}\dfrac{\partial}{\partial x} - \dfrac{1}{\overline{\rho}}\dfrac{\partial \mu}{\partial y}\dfrac{\partial}{\partial y} - \dfrac{1}{\overline{\rho}}\dfrac{\partial \mu}{\partial z}\dfrac{\partial}{\partial z} \\ \dfrac{\partial \overline{v}}{\partial x} - \dfrac{\mu}{\overline{\rho}}\dfrac{\partial^2}{\partial y \partial x} - \dfrac{1}{\overline{\rho}}\dfrac{\partial \mu}{\partial x}\dfrac{\partial}{\partial y} \\ \dfrac{\partial \overline{w}}{\partial x} - \dfrac{\mu}{\overline{\rho}}\dfrac{\partial^2}{\partial z \partial x} - \dfrac{1}{\overline{\rho}}\dfrac{\partial \mu}{\partial x}\dfrac{\partial}{\partial z} \\ \dfrac{\partial \overline{T}}{\partial x} + \dfrac{\overline{p}}{\overline{\rho}c_v}\dfrac{\partial}{\partial x} \\ \dfrac{\partial \overline{Y_1}}{\partial x} \end{pmatrix}, \tag{A2}$$

$$\begin{pmatrix} A_{\rho v} \\ A_{uv} \\ A_{vv} \\ A_{wv} \\ A_{Tv} \\ A_{Y_1 v} \end{pmatrix} = \begin{pmatrix} \overline{\rho}\dfrac{\partial}{\partial y} + \dfrac{\partial \overline{\rho}}{\partial y} \\ \dfrac{\partial \overline{u}}{\partial y} - \dfrac{\mu}{\overline{\rho}}\dfrac{\partial^2}{\partial x \partial y} - \dfrac{1}{\overline{\rho}}\dfrac{\partial \mu}{\partial y}\dfrac{\partial}{\partial x} \\ \dfrac{\partial \overline{v}}{\partial y} + \overline{u}\dfrac{\partial}{\partial x} + \overline{v}\dfrac{\partial}{\partial y} + \overline{w}\dfrac{\partial}{\partial z} - \dfrac{\mu}{\overline{\rho}}\left(\dfrac{\partial^2}{\partial x^2} + \dfrac{4}{3}\dfrac{\partial^2}{\partial y^2} + \dfrac{\partial^2}{\partial z^2}\right) - \dfrac{1}{\overline{\rho}}\dfrac{\partial \mu}{\partial x}\dfrac{\partial}{\partial x} - \dfrac{4}{3\overline{\rho}}\dfrac{\partial \mu}{\partial y}\dfrac{\partial}{\partial y} - \dfrac{1}{\overline{\rho}}\dfrac{\partial \mu}{\partial z}\dfrac{\partial}{\partial z} \\ \dfrac{\partial \overline{w}}{\partial y} - \dfrac{\mu}{\overline{\rho}}\dfrac{\partial^2}{\partial z \partial y} - \dfrac{1}{\overline{\rho}}\dfrac{\partial \mu}{\partial y}\dfrac{\partial}{\partial z} \\ \dfrac{\partial \overline{T}}{\partial y} + \dfrac{\overline{p}}{\overline{\rho}c_v}\dfrac{\partial}{\partial y} \\ \dfrac{\partial \overline{Y_1}}{\partial y} \end{pmatrix}, \tag{A3}$$

https://doi.org/10.1017/jfm.2026.11934 Published online by Cambridge University Press

$$\begin{pmatrix} A_{\rho w} \\ A_{uw} \\ A_{vw} \\ A_{ww} \\ A_{Tw} \\ A_{Y_1 w} \end{pmatrix} = \begin{pmatrix} \overline{\rho}\dfrac{\partial}{\partial z} + \dfrac{\partial \overline{\rho}}{\partial z} \\ \dfrac{\partial \overline{u}}{\partial z} - \dfrac{\mu}{\overline{\rho}}\dfrac{\partial^2}{\partial x \partial z} - \dfrac{1}{\overline{\rho}}\dfrac{\partial \mu}{\partial z}\dfrac{\partial}{\partial x} \\ \dfrac{\partial \overline{v}}{\partial z} - \dfrac{\mu}{\overline{\rho}}\dfrac{\partial^2}{\partial y \partial z} - \dfrac{1}{\overline{\rho}}\dfrac{\partial \mu}{\partial z}\dfrac{\partial}{\partial y} \\ \dfrac{\partial \overline{w}}{\partial z} + \overline{u}\dfrac{\partial}{\partial x} + \overline{v}\dfrac{\partial}{\partial y} + \overline{w}\dfrac{\partial}{\partial z} - \dfrac{\mu}{\overline{\rho}}\left(\dfrac{\partial^2}{\partial x^2} + \dfrac{\partial^2}{\partial y^2} + \dfrac{4}{3}\dfrac{\partial^2}{\partial z^2}\right) - \dfrac{1}{\overline{\rho}}\dfrac{\partial \mu}{\partial x}\dfrac{\partial}{\partial x} - \dfrac{1}{\overline{\rho}}\dfrac{\partial \mu}{\partial y}\dfrac{\partial}{\partial y} - \dfrac{4}{3\overline{\rho}}\dfrac{\partial \mu}{\partial z}\dfrac{\partial}{\partial z} \\ \dfrac{\partial \overline{T}}{\partial z} + \dfrac{\overline{p}}{\overline{\rho} c_v}\dfrac{\partial}{\partial z} \\ \dfrac{\partial \overline{Y_1}}{\partial z} \end{pmatrix}, \tag{A4}$$

$$\begin{pmatrix} A_{\rho T} \\ A_{uT} \\ A_{vT} \\ A_{wT} \\ A_{TT} \\ A_{Y_1 T} \end{pmatrix} = \begin{pmatrix} 0 \\ ZR\dfrac{\partial}{\partial x} \\ ZR\dfrac{\partial}{\partial y} \\ ZR\dfrac{\partial}{\partial z} \\ \overline{u}\dfrac{\partial}{\partial x} + \overline{v}\dfrac{\partial}{\partial y} + \overline{w}\dfrac{\partial}{\partial z} + \dfrac{ZR}{c_v}\left(\dfrac{\partial \overline{u}}{\partial x} + \dfrac{\partial \overline{v}}{\partial y} + \dfrac{\partial \overline{w}}{\partial z}\right) + \dfrac{\lambda}{\overline{\rho} c_v}\left(\dfrac{\partial^2}{\partial x^2} + \dfrac{\partial^2}{\partial y^2} + \dfrac{\partial^2}{\partial z^2}\right) + \dfrac{1}{\overline{\rho} c_v}\left(\dfrac{\partial \lambda}{\partial x}\dfrac{\partial}{\partial x} + \dfrac{\partial \lambda}{\partial y}\dfrac{\partial}{\partial y} + \dfrac{\partial \lambda}{\partial z}\dfrac{\partial}{\partial z}\right) \\ 0 \end{pmatrix}, \tag{A5}$$

$$\begin{pmatrix} A_{\rho Y_1} \\ A_{uY_1} \\ A_{vY_1} \\ A_{wY_1} \\ A_{TY_1} \\ A_{Y_1 Y_1} \end{pmatrix} = \begin{pmatrix} 0 \\ 0 \\ 0 \\ 0 \\ 0 \\ \overline{u}\dfrac{\partial}{\partial x} + \overline{v}\dfrac{\partial}{\partial y} + \overline{w}\dfrac{\partial}{\partial z} - \dfrac{D}{\overline{\rho}}\left(\dfrac{\partial \overline{\rho}}{\partial x}\dfrac{\partial}{\partial x} + \dfrac{\partial \overline{\rho}}{\partial y}\dfrac{\partial}{\partial y} + \dfrac{\partial \overline{\rho}}{\partial z}\dfrac{\partial}{\partial z}\right) - D\left(\dfrac{\partial^2}{\partial x^2} + \dfrac{\partial^2}{\partial y^2} + \dfrac{\partial^2}{\partial z^2}\right) - \dfrac{\partial D}{\partial x}\dfrac{\partial}{\partial x} - \dfrac{\partial D}{\partial y}\dfrac{\partial}{\partial y} - \dfrac{\partial D}{\partial z}\dfrac{\partial}{\partial z} \end{pmatrix}. \tag{A6}$$

In the incompressible-fluid algorithm, transforming equations (2.27) and (2.28) into the form of (2.23) yields the complete expression for $\boldsymbol{A}^*$. The resulting matrix has a dimension of $4\,\mathrm{m} \times 4\,\mathrm{m}$ – approximately half the size of the real-fluid operator – with its columns structured as follows:

$$\begin{pmatrix} A_{uu} \\ A_{vu} \\ A_{wu} \\ A_{pu} \end{pmatrix} = \begin{pmatrix} \dfrac{\partial \overline{u}}{\partial x} + \overline{u}\dfrac{\partial}{\partial x} + \overline{v}\dfrac{\partial}{\partial y} + \overline{w}\dfrac{\partial}{\partial z} - \dfrac{\mu}{\rho}\left(\dfrac{\partial^2}{\partial x^2} + \dfrac{\partial^2}{\partial y^2} + \dfrac{\partial^2}{\partial z^2}\right) \\ \dfrac{\partial \overline{v}}{\partial x} \\ \dfrac{\partial \overline{w}}{\partial x} \\ -\dfrac{\partial}{\partial x} \end{pmatrix}, \tag{A7}$$

https://doi.org/10.1017/jfm.2026.11934 Published online by Cambridge University Press

$$\begin{pmatrix} A_{uv} \\ A_{vv} \\ A_{wv} \\ A_{pv} \end{pmatrix} = \begin{pmatrix} \frac{\partial \overline{u}}{\partial y} \\ \frac{\partial \overline{v}}{\partial y} + \overline{u}\frac{\partial}{\partial x} + \overline{v}\frac{\partial}{\partial y} + \overline{w}\frac{\partial}{\partial z} - \frac{\mu}{\rho}\left(\frac{\partial^2}{\partial x^2} + \frac{\partial^2}{\partial y^2} + \frac{\partial^2}{\partial z^2}\right) \\ \frac{\partial \overline{w}}{\partial y} \\ -\frac{\partial}{\partial y} \end{pmatrix}, \tag{A8}$$

$$\begin{pmatrix} A_{uw} \\ A_{vw} \\ A_{ww} \\ A_{pw} \end{pmatrix} = \begin{pmatrix} \frac{\partial \overline{u}}{\partial z} \\ \frac{\partial \overline{v}}{\partial z} \\ \frac{\partial \overline{w}}{\partial z} + \overline{u}\frac{\partial}{\partial x} + \overline{v}\frac{\partial}{\partial y} + \overline{w}\frac{\partial}{\partial z} - \frac{\mu}{\rho}\left(\frac{\partial^2}{\partial x^2} + \frac{\partial^2}{\partial y^2} + \frac{\partial^2}{\partial z^2}\right) \\ -\frac{\partial}{\partial z} \end{pmatrix}, \tag{A9}$$

$$\begin{pmatrix} A_{up} \\ A_{vp} \\ A_{wp} \\ A_{pp} \end{pmatrix} = \begin{pmatrix} \frac{1}{\rho}\frac{\partial}{\partial x} \\ \frac{1}{\rho}\frac{\partial}{\partial y} \\ \frac{1}{\rho}\frac{\partial}{\partial z} \\ 0 \end{pmatrix}. \tag{A10}$$

In the operator matrix $\boldsymbol{A}$, the spatial discretisation of each gradient term is computed using the second-order central difference scheme. For instance, the gradient of u is calculated as

$$\left(\frac{\partial \overline{u}}{\partial x}\right)_{i,j,k} = \frac{\overline{u}_{i+1,j,k} - \overline{u}_{i-1,j,k}}{2\Delta x}, \tag{A11}$$

$$\left(\frac{\partial^2 \overline{u}}{\partial x^2}\right)_{i,j,k} = \frac{\overline{u}_{i+1,j,k} - 2\overline{u}_{i,j,k} + \overline{u}_{i-1,j,k}}{\Delta x^2}, \tag{A12}$$

$$\left(\frac{\partial^2 \overline{u}}{\partial x \partial y}\right)_{i,j,k} = \frac{\overline{u}_{i+1,j+1,k} - \overline{u}_{i+1,j-1,k} - \overline{u}_{i-1,j+1,k} + \overline{u}_{i-1,j-1,k}}{4\Delta x \Delta y}, \tag{A13}$$

where the subscripts i, j and k denote the spatial coordinate indices in the x, y and z directions, respectively.

Appendix B. Linear operator without diffusion terms

If the diffusion term is neglected, the componentwise form of the real-fluid linear operator $\boldsymbol{A}$ can be expressed as

https://doi.org/10.1017/jfm.2026.11934 Published online by Cambridge University Press

$$\begin{pmatrix} A_{\rho\rho} \\ A_{u\rho} \\ A_{v\rho} \\ A_{w\rho} \\ A_{T\rho} \\ A_{Y_1\rho} \end{pmatrix} = \begin{pmatrix} \frac{\partial \overline{u}}{\partial x} + \frac{\partial \overline{v}}{\partial y} + \frac{\partial \overline{w}}{\partial z} + \overline{u}\frac{\partial}{\partial x} + \overline{v}\frac{\partial}{\partial y} + \overline{w}\frac{\partial}{\partial z} \\ -\frac{1}{\overline{\rho}^2}\frac{\partial \overline{p}}{\partial x} + \frac{Z\overline{R}\overline{T}}{\overline{\rho}}\frac{\partial}{\partial x} \\ -\frac{1}{\overline{\rho}^2}\frac{\partial \overline{p}}{\partial y} + \frac{Z\overline{R}\overline{T}}{\overline{\rho}}\frac{\partial}{\partial y} \\ -\frac{1}{\overline{\rho}^2}\frac{\partial \overline{p}}{\partial z} + \frac{Z\overline{R}\overline{T}}{\overline{\rho}}\frac{\partial}{\partial z} \\ \left(\frac{Z\overline{R}\overline{T}}{\overline{\rho}c_v} - \frac{\overline{p}}{\overline{\rho}^2 c_v}\right)\left(\frac{\partial \overline{u}}{\partial x} + \frac{\partial \overline{v}}{\partial y} + \frac{\partial \overline{w}}{\partial z}\right) \\ 0 \end{pmatrix}, \tag{B1}$$

$$\begin{pmatrix} A_{\rho u} \\ A_{uu} \\ A_{vu} \\ A_{wu} \\ A_{Tu} \\ A_{Y_1 u} \end{pmatrix} = \begin{pmatrix} \overline{\rho}\frac{\partial}{\partial x} + \frac{\partial \overline{\rho}}{\partial x} \\ \frac{\partial \overline{u}}{\partial x} + \overline{u}\frac{\partial}{\partial x} + \overline{v}\frac{\partial}{\partial y} + \overline{w}\frac{\partial}{\partial z} \\ \frac{\partial \overline{v}}{\partial x} \\ \frac{\partial \overline{w}}{\partial x} \\ \frac{\partial \overline{T}}{\partial x} + \frac{\overline{p}}{\overline{\rho}c_v}\frac{\partial}{\partial x} \\ \frac{\partial \overline{Y_1}}{\partial x} \end{pmatrix}, \tag{B2}$$

$$\begin{pmatrix} A_{\rho v} \\ A_{uv} \\ A_{vv} \\ A_{wv} \\ A_{Tv} \\ A_{Y_1 v} \end{pmatrix} = \begin{pmatrix} \overline{\rho}\frac{\partial}{\partial y} + \frac{\partial \overline{\rho}}{\partial y} \\ \frac{\partial \overline{u}}{\partial y} \\ \frac{\partial \overline{v}}{\partial y} + \overline{u}\frac{\partial}{\partial x} + \overline{v}\frac{\partial}{\partial y} + \overline{w}\frac{\partial}{\partial z} \\ \frac{\partial \overline{w}}{\partial y} \\ \frac{\partial \overline{T}}{\partial y} + \frac{\overline{p}}{\overline{\rho}c_v}\frac{\partial}{\partial y} \\ \frac{\partial \overline{Y_1}}{\partial y} \end{pmatrix}, \tag{B3}$$

$$\begin{pmatrix} A_{\rho w} \\ A_{uw} \\ A_{vw} \\ A_{ww} \\ A_{Tw} \\ A_{Y_1 w} \end{pmatrix} = \begin{pmatrix} \overline{\rho}\frac{\partial}{\partial z} + \frac{\partial \overline{\rho}}{\partial z} \\ \frac{\partial \overline{u}}{\partial z} \\ \frac{\partial \overline{v}}{\partial z} \\ \frac{\partial \overline{w}}{\partial z} + \overline{u}\frac{\partial}{\partial x} + \overline{v}\frac{\partial}{\partial y} + \overline{w}\frac{\partial}{\partial z} \\ \frac{\partial \overline{T}}{\partial z} + \frac{\overline{p}}{\overline{\rho}c_v}\frac{\partial}{\partial z} \\ \frac{\partial \overline{Y_1}}{\partial z} \end{pmatrix}, \tag{B4}$$

https://doi.org/10.1017/jfm.2026.11934 Published online by Cambridge University Press

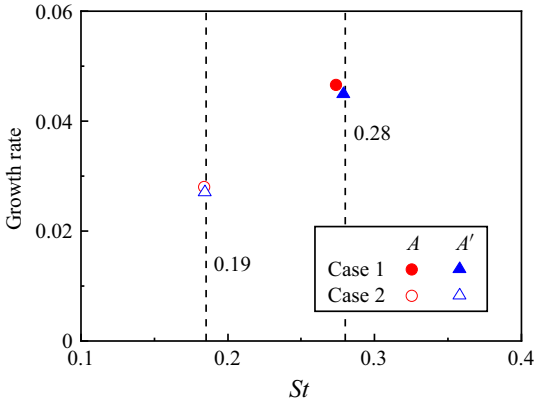


Figure 24. The GLSA eigenvalue spectrum for cases 1 and 2, obtained by linear operators with and without diffusion terms.

$$\begin{pmatrix} A_{\rho T} \\ A_{uT} \\ A_{vT} \\ A_{wT} \\ A_{TT} \\ A_{Y_1 T} \end{pmatrix} = \begin{pmatrix} 0 \\ ZR\frac{\partial}{\partial x} \\ ZR\frac{\partial}{\partial y} \\ ZR\frac{\partial}{\partial z} \\ \overline{u}\frac{\partial}{\partial x} + \overline{v}\frac{\partial}{\partial y} + \overline{w}\frac{\partial}{\partial z} + \frac{ZR}{c_v}\left(\frac{\partial \overline{u}}{\partial x} + \frac{\partial \overline{v}}{\partial y} + \frac{\partial \overline{w}}{\partial z}\right) \\ 0 \end{pmatrix}, \tag{B5}$$

$$\begin{pmatrix} A_{\rho Y_1} \\ A_{uY_1} \\ A_{vY_1} \\ A_{wY_1} \\ A_{TY_1} \\ A_{Y_1 Y_1} \end{pmatrix} = \begin{pmatrix} 0 \\ 0 \\ 0 \\ 0 \\ 0 \\ \overline{u}\frac{\partial}{\partial x} + \overline{v}\frac{\partial}{\partial y} + \overline{w}\frac{\partial}{\partial z} \end{pmatrix}. \tag{B6}$$

Obviously, the matrix experiences a considerable reduction in complexity. Figure 24 compares the GLSA eigenvalues for the two real-fluid operators using the base-flow data from cases 1 and 2. The comparison is conducted based on the two red markers indicated in figure 16, where A' denotes the operator without the diffusion terms. The results demonstrate that the eigenvalues obtained from the two operators exhibit negligible differences, with relative deviations in magnitude of 1.7 % for case 1 and 0.4 % for case 2. When the diffusion term is neglected, the growth rate of the characteristic mode increases slightly. This is attributed to the omission of viscous dissipation effects. Furthermore, the comparison in figure 25 (using the same colourbar scale) demonstrates that the two operators yield nearly identical eigenmode shapes. These results confirm that neglecting the influence of viscosity and the associated diffusion terms on the flow field in the present GLSA is justified.

Additionally, to facilitate a quantitative comparison, figures 26 and 27 present examples comparing the time-averaged and fluctuating components of the convective and diffusive terms in the x-momentum equation, respectively. The fluctuating components are calculated following (2.16), where the root mean square of velocity serves as the estimate for the velocity fluctuation term. As shown, the magnitude of the convective term is of the

https://doi.org/10.1017/jfm.2026.11934 Published online by Cambridge University Press

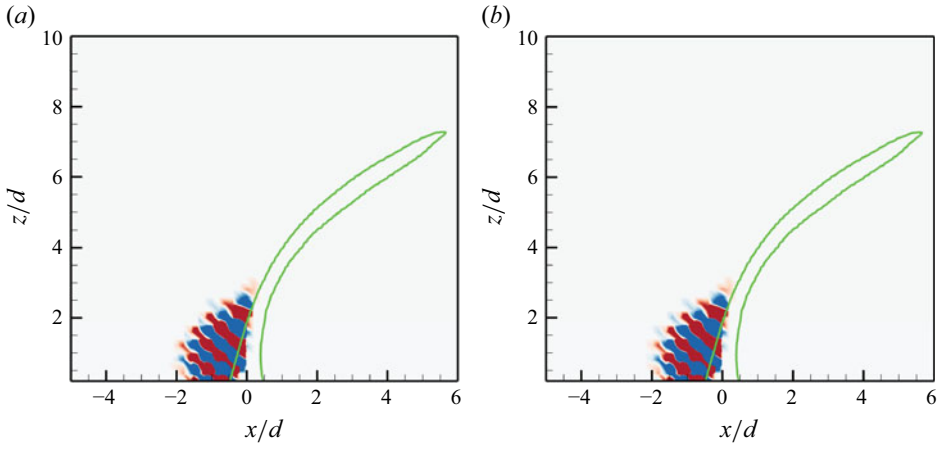


Figure 25. Real part of eigenmodes on jet-centre plane (case 1, $St = 0.28$), obtained by (a) a linear operator with diffusion terms, and (b) a linear operator without diffusion terms (positive and negative lumps: isocontours of $\tilde{w}$; green lines: isolines of $\overline{Y_1} = 0.7$).

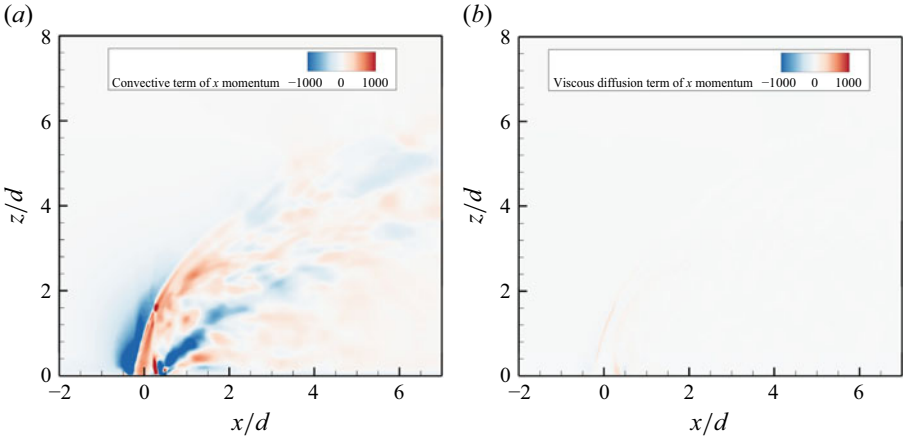


Figure 26. Spatial distributions of time-averaged x-momentum transport budgets on the jet-centre plane of case 1: (a) convective term, (b) viscous diffusion term (10).

order of 10^3, while that of the diffusive term is of the order of 10. Therefore, in cases 1–3, the influence of real-fluid transport coefficients on the flow-field characteristics and the GLSA results is relatively limited.

https://doi.org/10.1017/jfm.2026.11934 Published online by Cambridge University Press

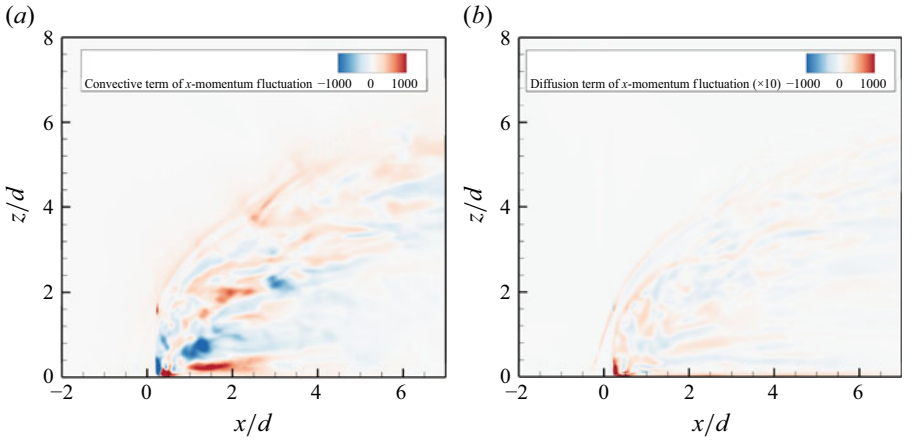


Figure 27. Spatial distributions of x-momentum fluctuation transport budgets on the jet-centre plane of case 1: (*a*) convective term, (*b*) viscous diffusion term (10).

References

Alves, L.S.D.B., Kelly, R.E. & Karagozian, A.R. 2007 Local stability analysis of an inviscid transverse jet. *J. Fluid Mech.* **581**, 401–418.

Alves, L.S.D.B., Kelly, R.E. & Karagozian, A.R. 2008 Transverse-jet shear-layer instabilities. Part 2. Linear analysis for large jet-to-crossflow velocity ratio. *J. Fluid Mech.* **602**, 383–401.

Amini, G. 2018 Linear stability analysis of a liquid jet in a weak crossflow. *Phys. Fluids* **30** (8), 084105.

Bagheri, S., Schlatter, P., Schmid, P.J. & Henningson, D.S. 2009 Global stability of a jet in crossflow. *J. Fluid Mech.* **624**, 33–44.

Barkley, D. 2006 Linear analysis of the cylinder wake mean flow. *Europhys. Lett.* **75** (5), 750–756.

Berkooz, G., Holmes, P. & Lumley, J.L. 1993 The proper orthogonal decomposition in the analysis of turbulent flows. *Annu. Rev. Fluid Mech.* **25** (1), 539–575.

Canton, J., Auteri, F. & Carini, M. 2017 Linear global stability of two incompressible coaxial jets. *J. Fluid Mech.* **824**, 886–911.

Cao, S., Hao, J., Guo, P., Wen, C.-Y. & Klioutchnikov, I. 2023*a* Stability of hypersonic flow over a curved compression ramp. *J. Fluid Mech.* **957**, A8.

Cao, Y., Xu, R., He, S. & Jiang, P. 2023*b* Accelerating turbulence in heated micron tubes at supercritical pressure. *J. Fluid Mech.* **972**, A13.

Chandh, A., Emerson, B. & Lieuwen, T. 2025 Evolution of shear layer vortices in jets in crossflow. In *AIAA SCITECH 2025 Forum*, p. 2754. American Institute of Aeronautics and Astronautics.

Dahms, R.N. & Oefelein, J.C. 2013 On the transition between two-phase and single-phase interface dynamics in multicomponent fluids at supercritical pressures. *Phys. Fluids* **25** (9), 092103.

Davitian, J., Getsinger, D., Hendrickson, C. & Karagozian, A.R. 2010 Transition to global instability in transverse-jet shear layers. *J. Fluid Mech.* **661**, 294–315.

Ding, S., Li, J. & Wang, X. 2024*b* Dynamics of elevated dodecane jets in crossflow at supercritical pressure. *Phys. Fluids* **36** (7), 075135.

Ding, S., Li, J., Wang, L., Ni, C. & Wang, X. 2024*a* Flow dynamics of a dodecane jet in oxygen crossflow at supercritical pressures. *AIAA J.* **62** (5), 1840–1853.

Fedioun, I. & Lardjane, N. 2005 Temporal linear stability analysis of three-dimensional compressible binary shear layers. *AIAA J.* **43** (1), 111–123.

Fu, Q. & Yang, L. 2016 Temporal instability of a transcritical shear layer. *J. Propul. Power* **32** (5), 1292–1297.

Fu, Q., Zhang, Y., Mo, C. & Yang, L. 2018 Instability of a shear layer between multicomponent fluids at supercritical pressure. *AIP Adv.* **8** (4), 045201.

Getsinger, D.R., Gevorkyan, L., Smith, O.I. & Karagozian, A.R. 2014 Structural and stability characteristics of jets in crossflow. *J. Fluid Mech.* **760**, 342–367.

Getsinger, D.R., Hendrickson, C. & Karagozian, A.R. 2012 Shear layer instabilities in low-density transverse jets. *Exp. Fluids* **53** (3), 783–801.

Gevorkyan, L., Shoji, T., Getsinger, D.R., Smith, O.I. & Karagozian, A.R. 2016 Transverse jet mixing characteristics. *J. Fluid Mech.* **790**, 237–274.

https://doi.org/10.1017/jfm.2026.11934 Published online by Cambridge University Press

GUARDONE, A., COLONNA, P., PINI, M. & SPINELLI, A. 2024 Nonideal compressible fluid dynamics of dense vapors and supercritical fluids. *Annu. Rev. Fluid Mech.* **56** (1), 241–269.

GUIHO, F., ALIZARD, F. & ROBINET, J.-C. 2013 Global stability analysis with compressible CFD solver. In *43rd Fluid Dynamics Conference*. American Institute of Aeronautics and Astronautics.

HAO, J., CAO, S., WEN, C.-Y. & OLIVIER, H. 2021 Occurrence of global instability in hypersonic compression corner flow. *J. Fluid Mech.* **919**, A4.

HUBER, M.L., LEMMON, E.W., BELL, I.H. & MCLINDEN, M.O. 2022 The NIST REFPROP database for highly accurate properties of industrially important fluids. *Ind. Engng Chem. Res.* **61** (42), 15449–15472.

HUERRE, P. & MONKEWITZ, P.A. 1990 Local and global instabilities in spatially developing flows. *Annu. Rev. Fluid Mech.* **22** (1), 473–537.

IYER, P.S. & MAHESH, K. 2016 A numerical study of shear layer characteristics of low-speed transverse jets. *J. Fluid Mech.* **790**, 275–307.

KARAGOZIAN, A.R. 2010 Transverse jets and their control. *Prog. Energy Combust. Sci.* **36** (5), 531–553.

KARAGOZIAN, A.R. 2014 The jet in crossflow. *Phys. Fluids* **26** (10), 101303.

KERVIK, E., HPFFNER, J., EHRENSTEIN, U.W.E. & HENNINGSON, D.S. 2007 Optimal growth, model reduction and control in a separated boundary-layer flow using global eigenmodes. *J. Fluid Mech.* **579**, 305–314.

KUMAR, G., BERTSCH, R.L. & GIRIMAJI, S.S. 2014 Stabilizing action of pressure in homogeneous compressible shear flows: effect of mach number and perturbation obliqueness. *J. Fluid Mech.* **760**, 540–566.

LEHOUCQ, R.B., SORENSEN, D.C. & YANG, C. 1998 *ARPACK Users' Guide: Solution of Large-Scale Eigenvalue Problems with Implicitly Restarted Arnoldi Methods*. SIAM.

LI, X. & SOTERIOU, M.C. 2018 Detailed numerical simulation of liquid jet atomization in crossflow of increasing density. *Intl J. Multiphase Flow* **104**, 214–232.

LIU, S., CHEN, X., WAN, B., ZHANG, L. & CHEN, J. 2024 Nonmodal linear stability analysis of hypersonic flow over an inclined cone. *Phys. Fluids* **36** (8), 084107.

LOPEZ-ECHEVERRY, J.S., REIF-ACHERMAN, S. & ARAUJO-LOPEZ, E. 2017 Peng-Robinson equation of state: 40 years through cubics. *Fluid Phase Equilib.* **447**, 39–71.

LUO, X., LI, M., DING, J., ZHAI, Z. & SI, T. 2019 Nonlinear behaviour of convergent Richtmyer–Meshkov instability. *J. Fluid Mech.* **877**, 130–141.

MAHESH, K. 2013 The interaction of jets with crossflow. *Annu. Rev. Fluid Mech.* **45** (1), 379–407.

MEGERIAN, S., DAVITIAN, J., DE, B., L., S. & KARAGOZIAN, A.R. 2007 Transverse-jet shear-layer instabilities. Part 1. Experimental studies. *J. Fluid Mech.* **593**, 93–129.

MENG, H., HSIAO, G.C., YANG, V. & SHUEN, J.S. 2005 Transport and dynamics of liquid oxygen droplets in supercritical hydrogen streams. *J. Fluid Mech.* **527**, 115–139.

MENG, H. & YANG, V. 2003 A unified treatment of general fluid thermodynamics and its application to a preconditioning scheme. *J. Comput. Phys.* **189** (1), 277–304.

MILLER, R.S., HARSTAD, K.G. & BELLAN, J. 2001 Direct numerical simulations of supercritical fluid mixing layers applied to heptane–nitrogen. *J. Fluid Mech.* **436**, 1–39.

M'CLOSKEY, R.T., KING, J.M., CORTELEZZI, L. & KARAGOZIAN, A.R. 2002 The actively controlled jet in crossflow. *J. Fluid Mech.* **452**, 325–335.

NARAYANAN, S., BAROOAH, P. & COHEN, J.M. 2003 Dynamics and control of an isolated jet in crossflow. *AIAA J.* **41** (12), 2316–2330.

OBRIST, D. & SCHMID, P.J. 2003 On the linear stability of swept attachment-line boundary layer flow. Part 1. Spectrum and asymptotic behaviour. *J. Fluid Mech.* **493**, 1–29.

OEFELEIN, J.C. 2005 Thermophysical characteristics of shear-coaxial LOX–H_2 flames at supercritical pressure. *Proc. Combust. Inst.* **30** (2), 2929–2937.

OKONGO, N. & BELLAN, J. 2003 Real-gas effects on mean flow and temporal stability of binary-species mixing layers. *AIAA J.* **41** (12), 2429–2443.

OKONG'O, N.A. & BELLAN, J. 2002 Direct numerical simulation of a transitional supercritical binary mixing layer: heptane and nitrogen. *J. Fluid Mech.* **464**, 1–34.

PEPLINSKI, A., SCHLATTER, P. & HENNINGSON, D.S. 2015 Global stability and optimal perturbation for a jet in cross-flow. *Eur. J. Mech. B. Fluids* **49**, 438–447.

PIERREHUMBERT, R.T. & WIDNALL, S. 1982 The two-and three-dimensional instabilities of a spatially periodic shear layer. *J. Fluid Mech.* **114**, 59–82.

POLING, B.E., PRAUSNITZ, J.M. & O'CONNELL, J.P. 2001 *The Properties of Gases and Liquids*, vol. 5. Mcgraw-hill.

REGAN, M.A. & MAHESH, K. 2017 Global linear stability analysis of jets incross-flow. *J. Fluid Mech.* **828**, 812–836.

https://doi.org/10.1017/jfm.2026.11934 Published online by Cambridge University Press

REN, J., FU, S. & PECNIK, R. 2018 Linear instability of poiseuille flows with highly non-ideal fluids. *J. Fluid Mech.* **859**, 89–125.
REN, J., MARXEN, O. & PECNIK, R. 2019 Boundary-layer stability of supercritical fluids in the vicinity of the Widom line. *J. Fluid Mech.* **871**, 831–864.
ROBERTS, M.S. & JACOBS, J.W. 2015 The effects of forced small-wavelength, finite-bandwidth initial perturbations and miscibility on the turbulent Rayleigh–Taylor instability. *J. Fluid Mech.* **787**, 50–83.
SCHMIDT, O.T. & RIST, U. 2011 Linear stability of compressible flow in a streamwise corner. *J. Fluid Mech.* **688**, 569–590.
SHAPIRO, S.R., KING, J.M., M'CLOSKEY, R.T. & KARAGOZIAN, A.R. 2006 Optimization of controlled jets in crossflow. *AIAA J.* **44** (6), 1292–1298.
SHOJI, T., HARRIS, E.W., BESNARD, A., SCHEIN, S.G. & KARAGOZIAN, A.R. 2020 On the origins of transverse jet shear layer instability transition. *J. Fluid Mech.* **890**, A7.
SIPP, D. & LEBEDEV, A. 2007 Global stability of base and mean flows: a general approach and its applications to cylinder and open cavity flows. *J. Fluid Mech.* **593**, 333–358.
STRYKOWSKI, P.J. & NICCUM, D.L. 1992 The influence of velocity and density ratio on the dynamics of spatially developing mixing layers. *Phys. Fluids A: Fluid Dyn.* **4** (4), 770–781.
THEOFILIS, V. 2011 Global linear instability. *Annu. Rev. Fluid Mech.* **43** (1), 319–352.
TURTON, S.E., TUCKERMAN, L.S. & BARKLEY, D. 2015 Prediction of frequencies in thermosolutal convection from mean flows. *Phys. Rev. E* **91** (4), 043009.
UNNIKRISHNAN, U., HUO, H., WANG, X. & YANG, V. 2021 Subgrid scale modeling considerations for large eddy simulation of supercritical turbulent mixing and combustion. *Phys. Fluids* **33** (7), 075112.
WAN, T., WANG, X.J., JIN, Y.X. & ZHAO, P.H. 2025 Effects of large density variations on near-wall turbulence and heat transfer in channel flow at supercritical pressure. *J. Fluid Mech.* **1007**, A68.
WANG, X., HUO, H., UNNIKRISHNAN, U. & YANG, V. 2018 A systematic approach to high-fidelity modeling and efficient simulation of supercritical fluid mixing and combustion. *Combust. Flame* **195**, 203–215.
WANG, X., LIU, T., MA, D. & YANG, V. 2022 Linear stability of real-fluid mixing layers at supercritical pressures. *Phys. Fluids* **34** (8), 084106.
WANG, X., WANG, Y. & YANG, V. 2019 Three-dimensional flow dynamics and mixing in a gas-centered liquid-swirl coaxial injector at supercritical pressure. *Phys. Fluids* **31** (6), 065109.
WANG, X. & YANG, V. 2017 Supercritical mixing and combustion of liquid-oxygen/ kerosene bi-swirl injectors. *J. Propul. Power* **33** (2), 316–322.
WHITE, M.T., BIANCHI, G., CHAI, L., TASSOU, S.A. & SAYMA, A.I. 2021 Review of supercritical CO_2 technologies and systems for power generation. *Appl. Therm. Engng* **185**, 116447.
XIE, G., XU, X., LEI, X., LI, Z., LI, Y. & SUNDEN, B. 2022 Heat transfer behaviors of some supercritical fluids: a review. *Chin. J. Aeronaut.* **35** (1), 290–306.
XUE, X., GAO, W., XU, Q., LIN, Y. & SUNG, C.-J. 2011 Injection of subcritical and supercritical aviation kerosene into a high-temperature and high-pressure crossflow. In *Turbo Expo: Power for Land, Sea, and Air*, vol. 54624, pp. 695–704. American Society of Mechanical Engineers.
YANG, V. 2000 Modeling of supercritical vaporization, mixing, and combustion processes in liquid-fueled propulsion systems. *Proc. Combust. Inst.* **28** (1), 925–942.
ZONG, N., MENG, H., HSIEH, S.-Y. & YANG, V. 2004 A numerical study of cryogenic fluid injection and mixing under supercritical conditions. *Phys. Fluids* **16** (12), 4248–4261.
ZONG, N. & YANG, V. 2007 Near-field flow and flame dynamics of LOX/methane shear-coaxial injector under supercritical conditions. *Proc. Combust. Inst.* **31** (2), 2309–2317.

https://doi.org/10.1017/jfm.2026.11934 Published online by Cambridge University Press